J. Appl. Comput. Mech., xx(x) (2026) 1-24
DOI: 10.22055/jacm.2026.49568.6081

ISSN: 2383-4536
jacm.scu.ac.ir

Shahid Chamran University of Ahvaz

Journal of Applied and Computational Mechanics



Research Paper

Thermal Performance Enhancement in Wavy Enclosures using Strategically Positioned Rectangular Blocks under Periodic Heating Conditions for Thermal Management Applications

Md Shohanur Rahman[1], Marzia Akter Mishu[1], Md. Aslam Hossain[1], Md. Azizur Rahman[1], G.M. Zahidul Islam[2], Md. Rezvi Hossain[1], Aftara Mehejabin[1]

[1] Department of Mathematics, Pabna University of Science and Technology, Pabna-6600, Bangladesh,
Email: mdshohanurrahmansiam888@gmail.com (Md.S.R.); marzia.math.pust@gmail.com (M.A.M.); aslam.math@pust.ac.bd (Md.A.H.); aziz@pust.ac.bd (Md.A.R.); mdrezvihossain2000@gmail.com (Md.R.H); afmehjabin@gmail.com (A.M.)

[2] General Education Department, University of Global Village, Barishal-8200, Bangladesh, Email: zahidbumath@gmail.com

Received July 14 2026; Revised October 07 2026; Accepted for publication October 12 2026.
✉ Corresponding author: Md. Aslam Hossain (aslam.math@pust.ac.bd)
© 2026 Published by Shahid Chamran University of Ahvaz

Abstract. Natural convection in enclosures with internal obstructions is central to thermal-management applications such as electronic cooling, solar receivers, and compact heat exchangers. This study numerically examines two-dimensional, steady laminar buoyancy-driven flow and heat transfer in a wavy square cavity containing a rectangular block at upper-left, center, and upper-right positions. The block is maintained at the cold reference temperature in Case I and at the hot reference temperature in Case II. The left and bottom wavy walls are subjected to periodic cosine temperature conditions, the right wavy wall is cold, and the top wall is adiabatic. The finite-element model is solved in COMSOL Multiphysics for Ra = 10^3–10^5 and Pr = 0.2, 0.71, and 10. Quantitative validation against published experimental data gives mean deviations of 4.97% and 3.93% on the two lateral walls. At the center position and Pr = 0.71, the dimensionless cut-line velocity magnitude increases from 0.3687 to 30.2837 in Case I and from 0.8110 to 34.9649 in Case II as Ra increases from 10^3 to 10^5. At Ra = 10^4 on the bottom wavy wall, changing the block from cold to heated at the coordinate-matched center position increases the average Nusselt number by 1.93-1.96%; the coordinate-matched upper-left change is marginal (-0.31% to -0.74%), while the case-specific upper-right configurations differ by -1.87% to -2.06%. These results show that block placement redistributes plume trajectories, recirculation, and wall-normal thermal gradients, so the preferred placement depends on the thermal-management objective rather than on a universal optimum.

Keywords: Natural convection, Wavy square cavity, Rectangular block, Nusselt number, Finite element method.

1. Introduction

Natural convection is the process of heat transportation that occurs in natural and engineering fields, in which the motion of fluid is not generated by the external force. Instead, the fluid motion occurs due to buoyancy. It is also known as free convection. When a fluid is heated, its density generally decreases, and the resulting buoyancy drives fluid motion that transports heat through the enclosure. Natural convection, a self-sustaining mode of heat transfer, has a broad spectrum of practical applications. Natural convection is used in many mechanical engineering systems to provide cooling. It is essential to HVAC (heating, ventilation, and air conditioning) systems in architectural and civil engineering for controlling building temperature. Heat generated by electrical components in electrical engineering can result in thermal stress and potential failure or malfunction. Natural convection is a key concept in chemical engineering that helps with reactor design, distillation procedures, and other heat and mass transfer systems. Natural convection in enclosures is essential for a variety of applications, such as materials processing, solar energy systems, inclined flat plate solar collectors, nuclear energy systems, and heat transmission through double-glazed windows, electronic cooling, and food sterilization.

Subhani and Kumar [1] investigated the effects of winglet insertion on a heated circular barrier. The study indicates that adding winglets to a heated circular barrier improves heat transfer and changes flow characteristics. Hayat Khan et al. [2] explored heat transfer and flow dynamics using sinusoidal wall temperature and an inclined plate. The results reveal that the inclined plate's amplitude, wavenumber, and thermal conditions influence heat transfer, entropy formation, and fluid dynamics. Mohebbi et al.'s research [3] focuses on the impact of barrier position inside a C-shaped enclosure on natural convection heat transfer. The study showed that larger Rayleigh numbers and uneven wall shapes promote convection and heat transfer. Khan et al. [4, 5] investigated

Published online: November 06 2026

mixed convection heat transport within a cavity with a square cylinder and hexagonal hollow obstruction. The study reported that the Rayleigh number (Ra) and Grashof number (Gr) significantly influence the Nusselt number, velocity, and kinetic-energy behavior. Fayz-Al-Asad et al. [6] investigated how natural convection within a triangle cavity is affected by a closed rectangular heat source. Findings are confirmed by previous studies and demonstrate that heat transfer rises with increasing Rayleigh numbers. Fluid temperature, Nusselt number, streamlines, velocity profiles, and isotherms are important outcomes.

Reviewing research on natural convection in porous media, Alturaihi et al. [7] highlighted how porosity and thermal conductivity affect heat transport. Boulahia et al. [8] investigated natural and mixed convection of nanofluids in rectangular wavy cavities with a focus on heat transmission and entropy generation. They found that higher Rayleigh numbers, nanoparticle fractions, and corrugated heater amplitudes enhance both heat transfer and entropy generation. El Moutaouakil et al. [9], Fayz-Al-Asad et al. [10], and Jasim Gumir et al. [11] conducted numerical analyses of natural convection and heat transfer in enclosure cavities; Jasim Gumir et al. [11] also considered a hybrid nanofluid. All of their outcomes show that increasing the Rayleigh number creates a bicellular flow and uniform temperature distribution, while fin length, wave amplitude, and wave number enhance heat transfer, and nanoparticle volume fraction and Darcy number affect flow and heat transfer in a porous cavity. Islam et al. [12] analysed the heatline visualization of heat transfer within a prismatic cavity filled with Cu-H_2O nanofluid. Heat transfer is improved by higher Rayleigh number, nanoparticle volume fraction, and Hartmann number. The heatline approach provides a better visualization of energy transfer, and various nanofluids are assessed for optimal performance. The development of nanofluids as high-performance thermal transport media has attracted substantial interest in heat-transfer research. Heat line visualization was also used by Alsabery et al. [13] to investigate convection in wavy enclosures. Heat transmission was improved with hybrid nanofluids. Amplitude and heat source impacts are analyzed in the study. Hybrid nanofluid in an enclosure with numerous heat sources in the presence of magnetic field is investigated by Chanda Roy [14]. The outcomes indicate that flow and heat transfer are influenced by the number of heat sources, Rayleigh number, and magnetic field, with higher Rayleigh numbers promoting flow and stronger magnetic fields slowing it. Giwa et al. [15] reviewed the effects of magnetic fields, nanofluid characteristics, and cavity conditions in square cavities on heat transfer in natural convection for applications in electronics and power plants. They find that magnetic fields have a significant impact on heat transfer and highlight novel ideas like bio-nanofluids. The study emphasizes new ideas in nanofluids and how they affect convective heat transfer in square cavities as it investigates the effects of magnetic fields, boundary conditions, governing parameters, and heat distribution on magnetohydrodynamic (MHD) natural convection. To investigate transient thermal behaviour in solid and fluid regions, Omidpanah et al. [16] used standard geometries to simulate flow and temperature distribution in hollow bricks. The study simulates heat flow in hollow bricks and examines thermal behavior using numerical techniques. It comes to the conclusion that bricks with vertical rectangular sub-cavities slow down heat transmission, especially when the emissivity of the wall is low, and that higher heat flow makes it take longer to reach steady-state conditions. Tayebi and Chamkha [17] studied the natural convection heat transfer of an Al_2O_3-Cu/water hybrid nanofluid in a square enclosure with a wavy conductive cylinder. The outcomes showed that the cylinder significantly affects flow patterns and heat transfer, allowing better thermal control.

Convection in cavities with an internal heat obstacle has received a lot of attention despite the use of nanofluids in heat transfer because of its practical applications. The impacts of magnetic hybrid nanoliquids (Al_2O_3-Cu/H_2O) and MHD convection on heat transport and entropy formation are highlighted in the study by Mliki and Abbassi [18]. The research results indicate that adding nanoparticles improves heat transfer while decreasing entropy generation; the average Nusselt number and entropy generation rise with higher Rayleigh numbers but decrease under a magnetic field. Tasnim et al. [19] showed that radiation enhances heat transport. According to their study, higher Rayleigh numbers promote heat transmission while Hartmann number hinders convection. An asymmetric heat source near the cold wall produced the lowest entropy and the best thermal performance. Using a nanofluid-filled porous trapezium-shaped cavity having localized baffles Zidan et al. [20] examined magneto-thermal convection. Their study investigated economic viability, entropy generation, and heat transmission, coming to the conclusion that nanofluids effectively and economically improve convection. Zheng et al. [21] investigated entropy generation and free convective heat transfer in an inclined enclosure with Al_2O_3-water nanofluid, along with the impact of external magnetic field and thermal radiation. The results demonstrate that the Nusselt number (Nu) and entropy generation increase with increasing Rayleigh number (Ra) and decreasing Hartmann number (Ha). Similar trends were reported by Dogonchi et al. [22], who numerically investigated free convection and thermal characteristics through a porous enclosure containing three circular cylinders. It was discovered that increasing Rayleigh number (Ra) & Darcy number (Da) and decreasing Hartmann number (Ha) strengthened the thermal-natural convective flow and overall heat transmission. Modifying the hot cylinder's relative position significantly alters the flow patterns of nanoliquids. The influence of the right angle of a triangular cavity on the natural convection of Cu-water nanofluid was studied numerically by Islam et al. [23]. They found that heat transmission and fluid flow are affected by the cavity angle. Moreover, their results indicate that the temperature transfer is inversely proportional to the Hartmann number while proportional to the buoyancy-driven parameter Rayleigh number. To study the thermal and hydraulic properties of a Casson-based multiwall carbon nanotube (MWCNT) nanofluid, some researchers [24-27] employed a closed wavy square. The enclosure is bounded by two cooled vertical walls and a wavy adiabatic top wall. According to their conclusions, the mean Nusselt number increases along the heated wavy wall with the Casson parameter, MWCNT volume fraction, Rayleigh number, and radiation parameter for all kinds of obstructions viewed thematically. The literature addresses three closely related strands including wavy-boundary natural convection, enclosure flows with internal obstacles, and non-uniform thermal forcing, which provide the physical basis for the present configuration.

Recent studies further emphasize the sensitivity of buoyancy-driven transport to corrugated or wavy boundaries and non-uniform thermal forcing. Es-Sabry et al. [28] examined natural convection in a corrugated-wall square cavity, while subsequent studies considered porous wavy cavities under partial magnetic forcing [29], wavy triangular cavities [30], and zigzag trapezoidal cavities [31]. Recent FEM-based thermal-management studies broaden this context further. Turabi et al. [32] examined double-diffusive natural convection and entropy generation in a multilayer trapezoidal solar receiver containing NEPCM together with porous and MHD effects; Turabi et al. [33] combined three-dimensional FEM with ANN prediction for a porous NEPCM solar-collector manifold. Akbar et al. [34] investigated magneto-radiative mixed convection in a lid-driven wavy square enclosure with a central heater, whereas Turabi et al. [35] coupled FEM and ANN for NEPCM-based thermal storage in a wavy porous triangular enclosure. These studies demonstrate the current emphasis on complex geometry, thermal storage, and data-assisted prediction, while also involving additional physics that differ from the single-fluid natural-convection framework considered here.

Against this background, the specific gap addressed here is not the use of FEM itself, but the absence of a controlled comparison that simultaneously combines three wavy enclosure walls, cosine thermal forcing on two mutually perpendicular walls, and the same relocatable rectangular block operated as either a heat sink or a heat source. Unlike the closely related studies [28–35], which employ fixed heaters or obstacles and/or additional porous, magnetic, radiative, phase-change, double-diffusive, or data-driven components, the present model deliberately isolates the interaction of block position and block thermal state within a classical

single-fluid buoyancy-driven system. The comparisons are performed under matched Ra, Pr, and wall conditions; where the same block coordinates are available, they are compared directly, while the case-specific upper-right coordinates are reported explicitly in Table 1 and are not interpreted as a pure one-factor thermal-state change.

1.1. Objective of the study

The primary objective of this study is to investigate the natural-convection heat transfer characteristics of a sinusoidally wavy enclosure subjected to spatially periodic heating and containing a strategically positioned rectangular block. Specifically, the study aims to:

(i) characterize the flow and thermal fields induced by the interaction of wavy boundaries and periodic thermal loading;
(ii) evaluate the effects of the block acting as an internal heat sink and heat source;
(iii) examine the influence of relocating the block among the upper-left, central, and upper-right positions;
(iv) quantify the resulting heat-transfer performance using local and average Nusselt numbers;
(v) elucidate the coupled effects of block location, thermal condition, and periodic heating on buoyancy-driven flow and heat-transfer pathways; and
(vi) identify favorable configurations that can provide useful design guidance for thermal-management systems involving non-uniform heating and internal components.

1.2. Novelty and scientific contribution

The present study extends the conventional analysis of natural convection in enclosures by considering the combined effects of sinusoidally wavy boundaries, spatially periodic thermal loading, and a strategically relocatable internal rectangular block. This configuration represents a more realistic thermal-management scenario than idealized cavities with uniformly heated walls and fixed obstacles. In particular, the study considers two complementary thermal states of the block: a cold block acting as an internal heat sink and a hot block acting as an internal heat source. The block is systematically positioned at the upper-left, center, and upper-right locations to determine how its proximity to different regions of the periodically heated and cold wavy boundaries alters the buoyancy-driven circulation, thermal stratification, and heat-transfer pathways. The novelty therefore lies not simply in varying the block position, but in revealing the coupled interaction between thermal non-uniformity, boundary waviness, obstacle location, and obstacle thermal state. The resulting analysis provides insight into whether an internal component should be positioned to enhance heat absorption or heat release and how its location can be exploited as a thermal-design parameter. These findings are particularly relevant to engineering systems involving non-uniform heating and internal obstructions, including solar-thermal collectors, heat exchangers, and compact thermal-management devices. The methodological contribution is therefore the controlled physical comparison of block location and thermal state under clearly specified operating conditions, rather than the introduction of a new finite-element algorithm.

2. Problem Statement

This study examines two-dimensional, steady, laminar natural convection of a generic incompressible Newtonian fluid ($Pr = 0.2, 0.71,$ and 10) within a square cavity of side $L = 1\ m$, bounded by three sinusoidally corrugated (wavy) walls and one flat wall, with a solid rectangular block of length $l = 0.3\ m$ and height $h = 0.1\ m$ embedded within the enclosure. The left and bottom walls are wavy and subjected to a spatially periodic, cosine-distributed heating profile, $(T_h - T_c)\cos(\pi x/L) + T_c$ and $(T_h - T_c)\cos(\pi y/L) + T_c$, respectively, representative of the non-uniform thermal loading encountered in practical solar-collector and heat-exchanger geometries. The right wavy wall is maintained at a uniform cold temperature Tc, and the top wall is thermally insulated. All cavity and block surfaces satisfy the no-slip velocity condition, and the reference pressure is taken as zero. Two complementary thermal scenarios are analyzed to capture both heat-absorbing and heat-generating obstructions relevant to thermal management applications. In Case I, the rectangular block is maintained at the cold-wall temperature ($\theta = 0$) and behaves as an internal heat sink; in Case II, the block is maintained at the hot-wall temperature ($\theta = 1$) and behaves as an internal heat source. In both cases, the block is successively relocated to the upper-left, center, and upper-right positions of the cavity to assess the influence of obstacle placement on the resulting flow and thermal fields.

The flow is governed by the steady, incompressible continuity, momentum, and energy equations, with the Boussinesq approximation employed to couple buoyancy forces to the temperature field. Using the cavity side length L as the characteristic length scale, α/L as the velocity scale, and $(T_h - T_c)$ as the temperature scale, these equations are cast into non-dimensional form in terms of the Rayleigh number, $Ra = g\beta(T_h - T_c)L^3/(\nu\alpha)$, and the Prandtl number, $Pr = \nu/\alpha$, subject to no-slip velocity conditions on all boundaries, the prescribed periodic thermal conditions on the left and bottom walls, an isothermal cold condition on the right wall, an adiabatic condition on the top wall, and $\theta = 0$ (Case I) or $\theta = 1$ (Case II) on the block surface. The resulting coupled, non-linear partial differential equations are solved using the finite element Galerkin weighted residual method, implemented in COMSOL Multiphysics, over the parametric range $10^3 \leq Ra \leq 10^5$, for free triangular meshes refined until grid-independent average Nusselt numbers were obtained.

The exact COMSOL thermal expressions are $\cos((\pi y)/L)$ on the left wavy wall, $\cos((\pi x)/L)$ on the bottom wavy wall, $T = 0$ on the right wavy wall, thermal insulation on the top wall, and $\theta = 0$ (Case I) or $\theta = 1$ (Case II) on the block. The calculations are restricted to the adopted two-dimensional steady laminar formulation over $10^3 \leq Ra \leq 10^5$; the onset of unsteadiness is geometry- and boundary-condition-dependent, so the conclusions are not extrapolated beyond this range. The geometric definitions, exact boundary expressions, and block positions are summarized in Table 1 and illustrated in Fig. 1. The cosine functions are used here as an idealized spatially periodic thermal forcing rather than as uniformly positive heating. Because $\theta = \frac{T-T_c}{T_h-T_c}$ a negative dimensionless temperature simply denotes a local prescribed wall temperature below the chosen reference T_c; it does not imply a negative absolute temperature. Accordingly, the term 'periodic heating' in this study refers to the imposed spatially varying thermal condition, which contains relatively warmer and cooler segments along the wavy walls.

3. Governing Equations & Boundary Conditions

All of the fluid's thermophysical characteristics are taken for granted in the flow model, with the exception of density fluctuations that result in a body force term in the momentum equation. According to Roy and Basak's research [25], the Boussinesq approximation is used for the fluid characteristics to couple the temperature field to the flow field and relate density changes to temperature changes.

Table 1. Geometric definitions, block positions, and COMSOL thermal boundary expressions.

Boundary	Definition	Boundary	Definition
Bottom wavy	$y = A[1 - \cos(2\pi\lambda x/L)]$	Left wavy	$x = A[\cos(2\pi\lambda y/L) - 1]$
Right wavy	$x = L + A[1 - \cos(2\pi\lambda y/L)]$	Top	$y = L$
Geometry	$A = 0.08L;\ \lambda = 3$	Block size	$l = 0.30L;\ H = 0.10L$
Block position	**x-coordinate**	**y-coordinate**	**Reference**
Upper left	$0.15L$	$0.90L$	Center
Center	$0.50L$	$0.50L$	Center
Upper right (Case II)	$0.80L$	$0.90L$	Center
Upper right (Case I)	$0.85L$	$0.90L$	Center

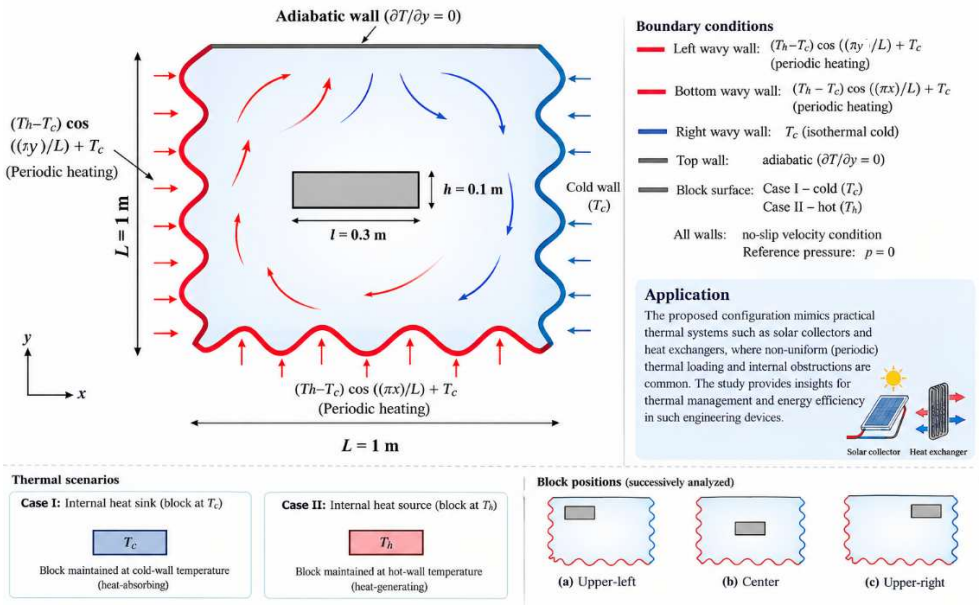


Fig. 1. Schematic configuration of the considered system and its applications.

Using the conservation of mass, momentum, and energy, the governing equations for steady natural convection flow are as follows:

The non-dimensional governing equations and boundary conditions are given by [25]:

$$\frac{\partial U}{\partial X} + \frac{\partial V}{\partial Y} = 0 \tag{1}$$

$$U\frac{\partial U}{\partial X} + V\frac{\partial U}{\partial Y} = -\frac{\partial P}{\partial X} + Pr\left(\frac{\partial^2 U}{\partial X^2} + \frac{\partial^2 U}{\partial Y^2}\right) \tag{2}$$

$$U\frac{\partial V}{\partial X} + V\frac{\partial V}{\partial Y} = -\frac{\partial P}{\partial Y} + Pr\left(\frac{\partial^2 V}{\partial X^2} + \frac{\partial^2 V}{\partial Y^2}\right) + Ra\,Pr\,\theta \tag{3}$$

$$U\frac{\partial \theta}{\partial X} + V\frac{\partial \theta}{\partial Y} = \left(\frac{\partial^2 \theta}{\partial X^2} + \frac{\partial^2 \theta}{\partial Y^2}\right) \tag{4}$$

The non-dimensional boundary conditions are:

$$U = V = 0 \text{ on all cavity walls and block surfaces} \tag{5}$$

$$\theta = \cos(\pi X) \text{ on the bottom wavy wall; } \theta = \cos(\pi Y) \text{ on the left wavy wall} \tag{6}$$

$$\theta = 0 \text{ on the right wavy wall; } \partial\theta/\partial Y = 0 \text{ on the top wall} \tag{7}$$

$$\text{On the block: } \theta = 0, U = V = 0 \text{ (Case I) and } \theta = 1, U = V = 0 \text{ (Case II)} \tag{8}$$

The periodic temperatures are evaluated pointwise on the actual wavy boundaries using the global dimensionless coordinates $X = x/L$ and $Y = y/L$. The corresponding dimensional COMSOL expressions are $\cos((\pi x)/L)$ on the bottom wall and $\cos((\pi y)/L)$ on the left wall, with $T = 0$ on the right wall and thermal insulation on the top wall.

Following Roy and Basak [25], the local Nusselt number is obtained from the temperature gradient normal to the wall, $Nu = -\partial\theta/\partial n$, where n is the unit normal pointing into the fluid and the minus sign follows the outward-normal convention. The average Nusselt number on each heated wavy wall (left and bottom) is calculated along the actual curved length of the wall:

$$Nu_{avg} = (1/S) \int_{\Gamma} (-\partial\theta/\partial n)\, dS \tag{9}$$

where dS is the arc-length element along the wall Γ and $S = \int_{\Gamma} dS$ is its actual length, so the projected length is not used. In COMSOL, this was done by applying the Boundary Average operator to each curved wall.

The set of non-dimensional variables used to get non-dimensional governing equations (1)-(4) and non-dimensional boundary conditions are given by:

$$X = \frac{x}{L}, Y = \frac{y}{L}, U = \frac{uL}{\alpha}, V = \frac{vL}{\alpha}, P = \frac{pL^2}{\rho\alpha^2}, \theta = \frac{T - T_c}{T_h - T_c} \tag{10}$$

4. Grid Independent Test and Mesh Generation

To ensure that the reported flow and thermal predictions are independent of the discretization employed, a systematic grid-sensitivity analysis was carried out at Ra = 10^4 and Pr = 0.71 using six progressively refined free-triangular meshes (G1–G6). The average Nusselt number was adopted as the monitoring variable, since it reflects the wall-normal temperature gradient along the thermally active boundaries and is therefore the most sensitive global indicator of solution accuracy. The corresponding Case I and Case II grid-independence results are summarized in Tables 2 and 3.

As summarized in Tables 2 and 3 and illustrated in Fig. 3, Nu rises only marginally beyond mesh G5 for both thermal configurations refining the mesh from G5 to G6 with an 26.2% increase in domain elements that changes Nu by a negligible 0.015% in Case I and produces no discernible change (0.000%) in Case II. This asymptotic convergence confirms that the solution has entered the grid-independent regime well before the finest mesh is reached, so that further refinement yields diminishing computational returns without any corresponding gain in accuracy. Mesh G5, comprising 30,508 domain elements and 1008 boundary elements (67,032 degrees of freedom, 46 s CPU time), was therefore adopted for all subsequent simulations, offering an optimal balance between numerical fidelity and computational economy. Figure 2 shows the resulting free-triangular mesh, with visibly denser clustering near the wavy walls and around the rectangular block, where steep velocity and temperature gradients are anticipated.

Table 2. Average Nusselt numbers for grid-independence test (Case I) at $Ra = 10^4$.

Mesh Size	No. of Elements		Nusselt Number, Nu	Number of Degree of Freedom	Computation time	Deviation in Nu (in %)
	Domain	Boundary				
G1	4447	319	3.2656	10776	24 s	-
G2	5478	346	3.2665	13000	20 s	0.028
G3	8324	429	3.2718	19184	21 s	0.162
G4	13002	560	3.2738	29332	26 s	0.061
G5	**30508**	**1008**	**3.2811**	**67032**	**46 s**	0.223
G6	38496	1008	3.2816	83008	54 s	**0.015**

Table 3. Average Nusselt numbers for grid-independence test (Case II) at $Ra = 10^4$.

Mesh Size	No. of Elements		Nusselt Number, Nu	Number of Degree of Freedom	Computation time	Deviation in Nu (in %)
	Domain	Boundary				
G1	4447	319	3.1804	10776	29 s	-
G2	5478	346	3.1803	13000	19 s	-0.003
G3	8324	429	3.1826	19184	21 s	0.072
G4	13002	560	3.1835	29332	28 s	0.028
G5	**30508**	**1008**	**3.1877**	**67032**	**46 s**	0.132
G6	38496	1008	3.1877	83008	55 s	**0**

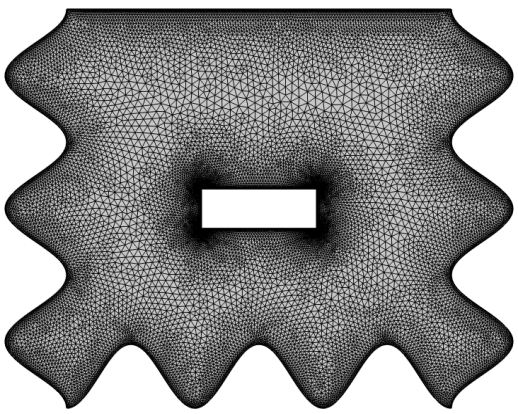


Fig. 2. Mesh generation of the cavity.

5. Methodology

The coupled, non-linear system of continuity, momentum, and energy equations, together with the associated boundary conditions, was solved using the finite-element Galerkin weighted-residual method, following the general procedure detailed by Zienkiewicz and Taylor [26]. The computational domain was discretized into non-overlapping triangular elements, over which the velocity and temperature fields were approximated by piecewise polynomial basis functions. Iterative convergence was enforced using the criterion $|\eta^{n+1} - \eta^{n}| \leq 10^{-5}$ where $n+1$ and n are two successive iterations and $\eta(U, V, \theta)$ denotes the value of the iterations. All simulations were performed in COMSOL Multiphysics, a finite-element platform well suited to the strongly coupled, non-linear buoyancy–momentum–energy interactions that characterize natural convection in geometrically complex enclosures.

For reproducibility, the simulations were performed in COMSOL Multiphysics 6.2 (Build 290) using the two-dimensional Laminar Flow and Heat Transfer in Fluids interfaces in a stationary parametric study. The saved model uses first-order Lagrange discretization, consistent streamline/crosswind stabilization, a fully coupled nonlinear formulation, and the PARDISO direct solver. The stationary relative tolerance is 10^{-3}, with a maximum of 100 nonlinear iterations, an initial damping factor of 0.01, a minimum step of 10^{-6}, and zero initial fields for u, v, T and p. No pseudo-time or parametric continuation strategy is activated. Selected corrected post-processing CSV files were exported after reopening the solved models in COMSOL 6.3.0.290 without changing the solution fields.

The overall solution procedure is summarized schematically in Fig. 4. The workflow proceeds sequentially from definition of the physical domain and governing equations, through specification of boundary conditions and material properties, to mesh generation and solution validation. At each stage, the simulation is advanced under the prescribed convergence tolerance. If convergence is not attained, the solution parameters are updated and the iteration repeated, whereas satisfaction of the convergence criterion permits extraction of the converged flow, thermal, and heat-transfer results. To reconcile the built-in vectorial formulation used internally by COMSOL with the non-dimensional Cartesian governing equations, the dimensionless groups (Ra, Pr) and the scaled field variables (U, V, θ, P) were mapped one-to-one onto the corresponding COMSOL input parameters, ensuring that the software-implemented equations reproduce exactly the non-dimensional model formulated for the present cavity–block configuration.

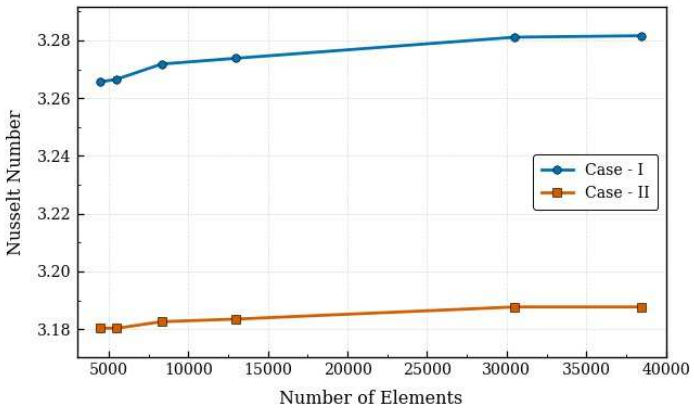


Fig. 3. Grid independence test.

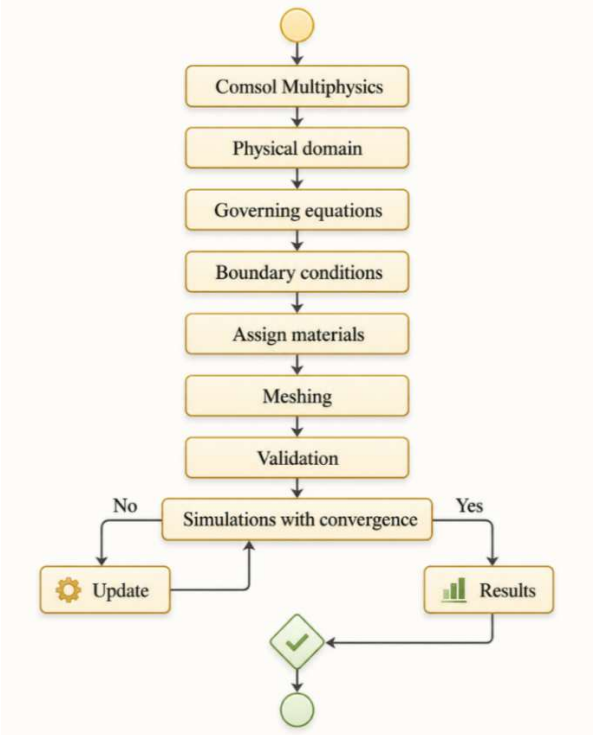


Fig. 4. Methodology flowchart.

6. Model Validation

Prior to undertaking the parametric investigation, the numerical framework was validated against an independent benchmark from the literature to establish confidence in the solution methodology. The validation problem considers buoyancy-driven convection of air within a triangular cavity containing a centrally embedded, uniformly heated rectangular obstruction; the two inclined side walls of the cavity are maintained at a constant cold temperature, while the top wall and all surfaces of the rectangular block are uniformly heated. This configuration was reproduced in COMSOL under identical geometric and thermal boundary conditions, and the resulting streamline and isotherm patterns were compared against the corresponding results reported by Fayz-Al-Asad et al. [6] for Ra = 10^4 and 10^5. The streamline and isotherm comparisons are presented in Figs. 5(a) and 5(b), respectively. As shown in Fig. 5(a), the present streamline topology reproduces the counter-rotating vortex pair reported in the benchmark study at both Rayleigh numbers, with the vortex cores forming

adjacent to the inclined walls and the flow strengthening and migrating toward the block as Ra increases from 10^4 to 10^5. The isotherm comparison in Fig. 5(b) likewise shows close qualitative agreement: temperature contours are compressed near the heated apex and along the block surface, consistent with the thinning of the thermal boundary layer expected at the higher Rayleigh number. The close correspondence between the present predictions and the published benchmark, across both the momentum and thermal fields and over an order-of-magnitude change in Ra, confirms that the finite-element formulation, mesh strategy, and solution procedure adopted in this study reliably capture the governing buoyancy-driven transport physics, thereby lending confidence to the parametric results presented in the following section.

To further enhance the credibility of the present work, additional comparisons were made with the experimental and numerical results of Paroncini et al. [27], as illustrated in Figs. 5(c) and 5(d). Velocity and isotherm profiles were examined together with a quantitative comparison against the results reported by Paroncini et al. [27]. Figures 5(c) and 5(d) show close agreement between the results of Paroncini et al. [27] and the present work. There is a negligible error due to mesh sensitivity and geometry dimensions sensitivity, as summarized in Table 4.

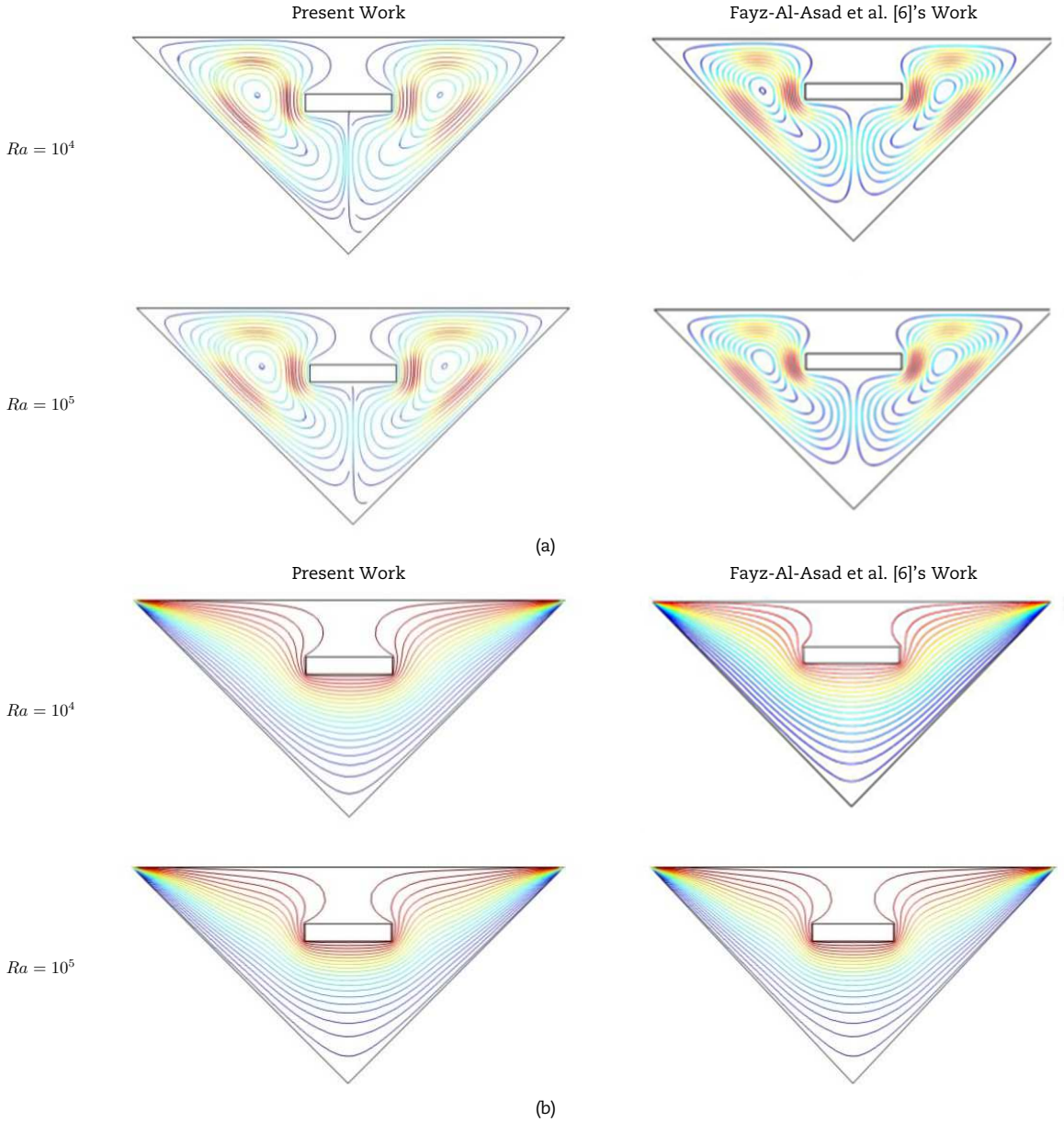
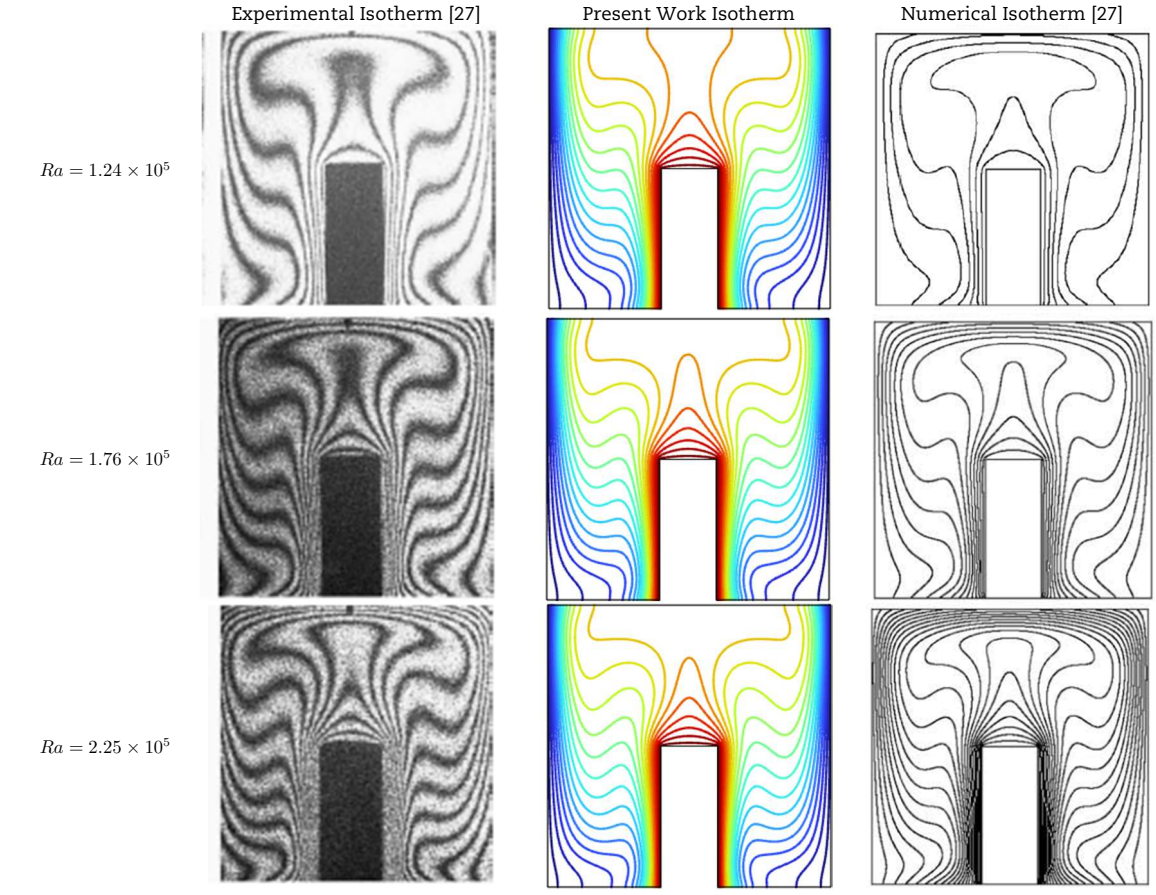
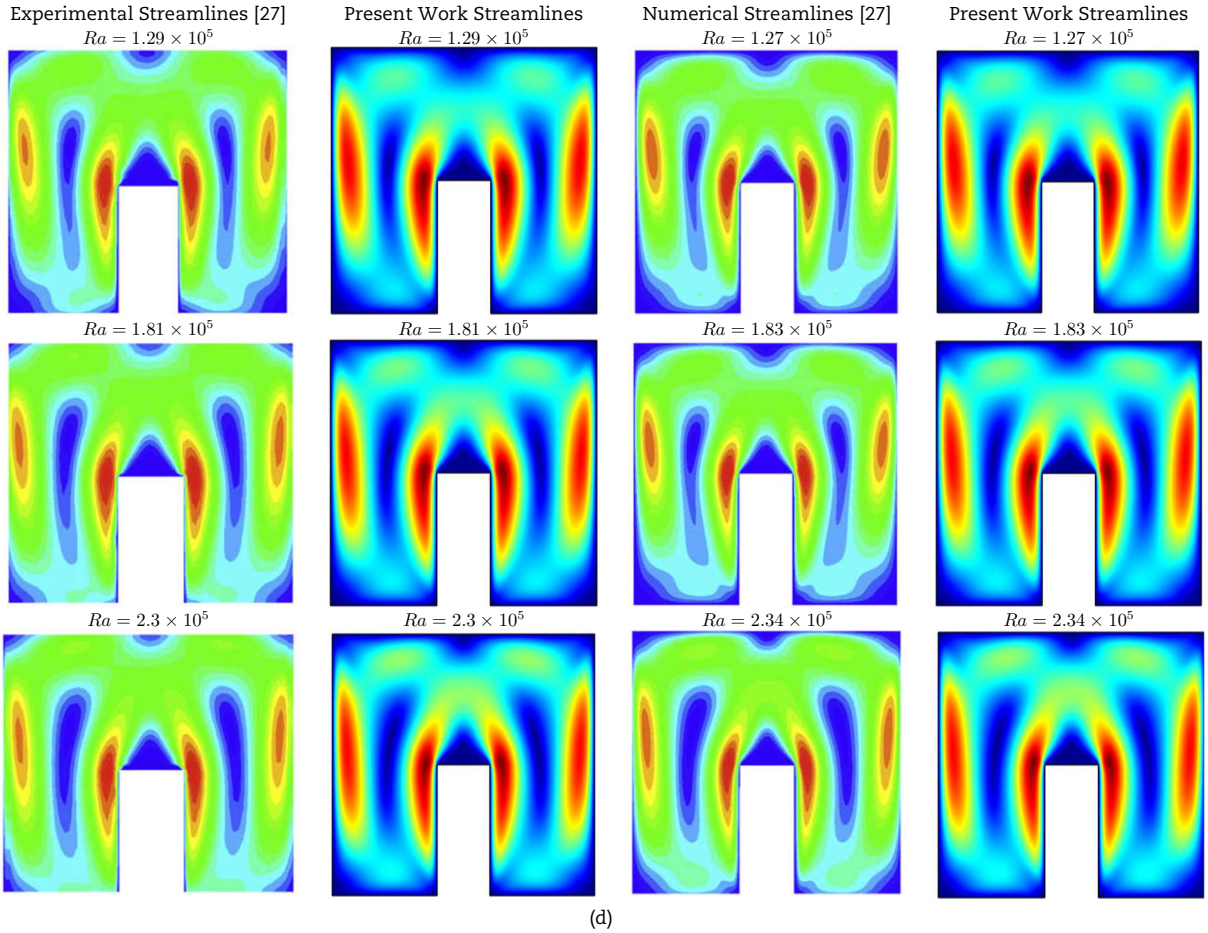


Fig. 5. (a) Streamlines and (b) Isotherms comparisons of the present work with Fayz-Al-Asad et al. [6], (c) Isotherm and (d) Streamline comparison of the present work with the experimental and numerical results of Paroncini et al. [27].



(c)



(d)

Fig. 5. Continued.

Table 4. Comparison of average Nusselt numbers at the lateral walls with Paroncini et al. [27] for $\zeta = 0.5$.

Ra	Nu_{rg}			Nu_{lf}		
	Exp. [27]	Num. [27]	Present	Exp. [27]	Num. [27]	Present
1.24×10^5	9.04	8.98	8.66	9.07	8.98	8.66
1.46×10^5	9.38	9.40	9.04	9.32	9.39	9.05
1.76×10^5	9.98	9.89	9.49	9.9	9.89	9.50
2.05×10^5	10.4	10.31	9.87	10.06	10.31	9.88
2.25×10^5	10.86	10.57	10.10	10.8	10.57	10.11

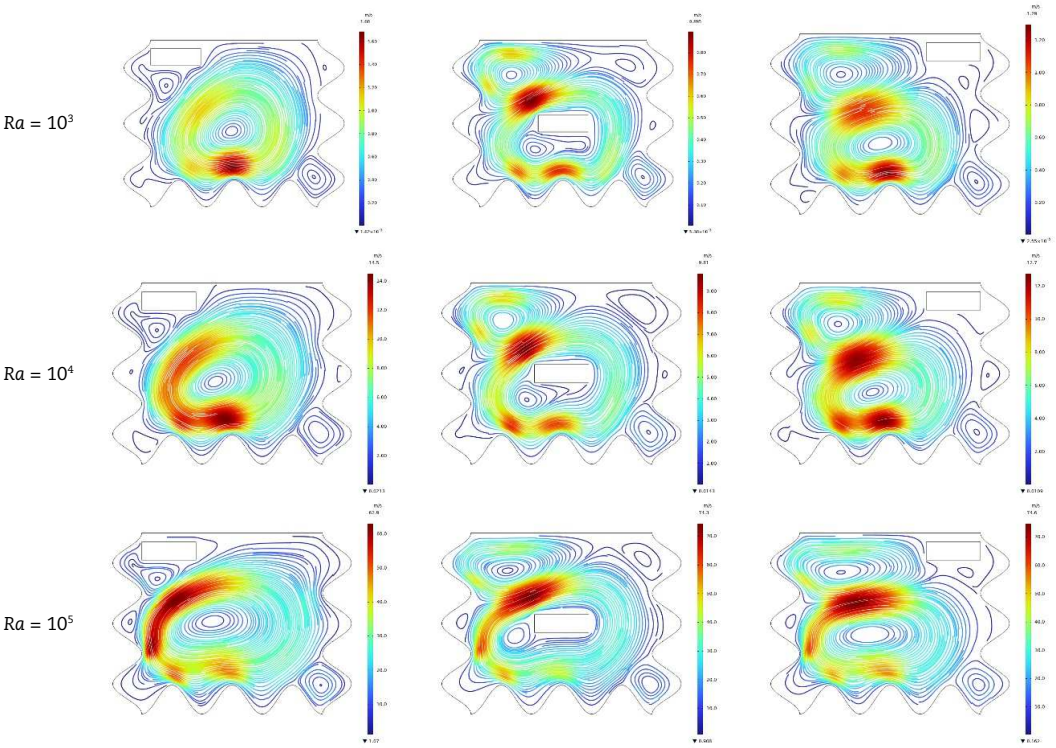


Fig. 6. Effects of Ra for different block positions on streamlines (Case I, dimensionless velocity magnitude) when Pr = 0.71.

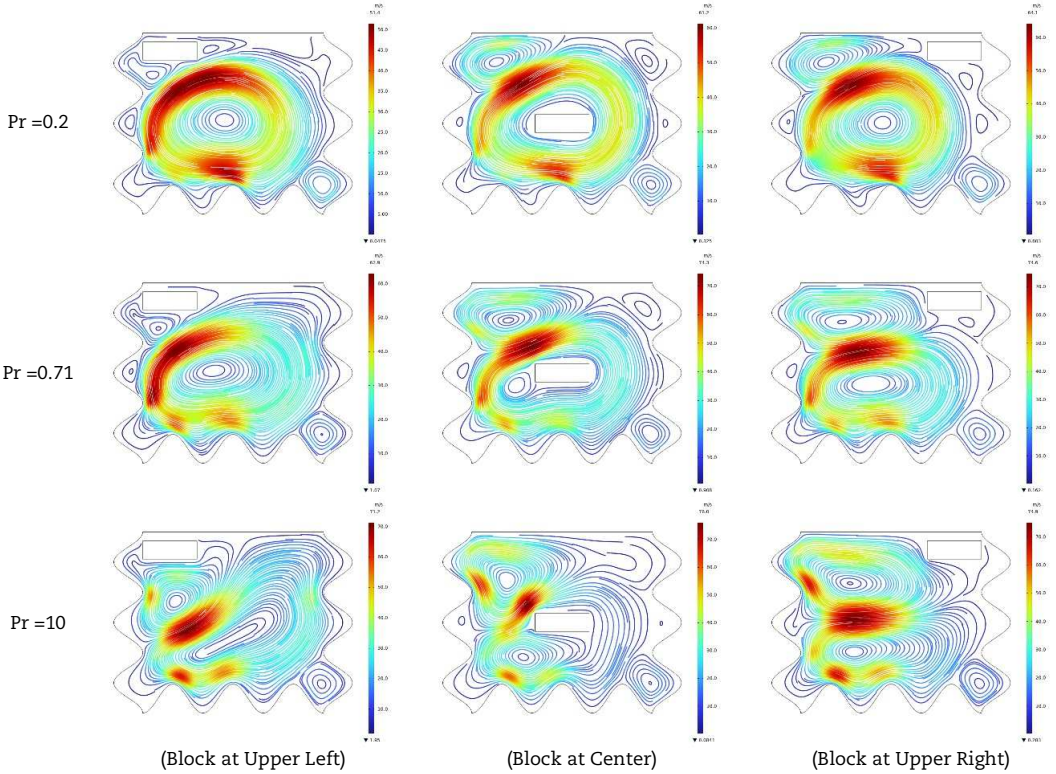


Fig. 7. Effects of Pr for different block positions on streamlines (Case I, dimensionless velocity magnitude) when Ra = 10^5.

For the lateral-wall average Nusselt number, the present results give the mean absolute percentage deviations of 4.97% (left wall) and 3.93% (right wall) relative to the experimental values of Paroncini et al. [27], with maximum deviations of 7.00% and 6.39%, respectively. Relative to their numerical values, the corresponding mean deviations are 4.03% and 3.93%, with maxima of 4.45% and 4.35%.

7. Results and Discussion

The buoyancy-driven flow and heat transfer characteristics of a generic incompressible Newtonian fluid (Pr = 0.2, 0.71, 10) confined within the wavy square cavity were examined over $10^3 \le Ra \le 10^5$, with the rectangular block successively located at the upper-left, center, and upper-right positions, and maintained either at the cold-wall temperature (Case I, heat sink) or the hot-wall temperature (Case II, heat source). The resulting streamline, isotherm, and heat-transfer characteristics are discussed below with emphasis on the physical mechanisms underlying the observed trends.

7.1. Effects on streamlines (Case I)

Figure 6 illustrates the influence of Ra on the flow field at Pr = 0.71. At $Ra = 10^3$, the buoyancy force is too weak to overcome viscous damping, and the flow organizes into a single mild circulation cell with weak velocity gradients.

The cold block introduces only a minor local perturbation to this pattern. As Ra increases through 10^4 to 10^5, the progressively stronger buoyancy force destabilizes the primary cell, giving rise to multiple interacting vortices and a markedly more spatially complex flow structure. Physically, this reflects the transition from a conduction-dominated to a convection-dominated transport regime. As the buoyancy-to-viscous force ratio grows, inertial effects increasingly dictate the flow topology, and the embedded block acts as a bluff obstruction that splits and redirects the developing plumes. At the center position and Pr = 0.71, the dimensionless cut-line velocity magnitude increases from 0.3687409821 at $Ra = 10^3$ to 30.2836881514 at $Ra = 10^5$, corresponding to an 8112.73% increase. This controlled comparison varies Ra only and keeps the block position and Pr fixed.

The corresponding Prandtl-number sensitivity is shown in Fig. 7 for $Ra = 10^5$. At Pr = 0.2, thermal disturbances diffuse rapidly relative to momentum, producing broad, diffuse vortices with gently varying velocity contours.

As Pr increases, the relative rates of momentum and thermal diffusion alter the confinement of the buoyancy-driven shear layers. At the center position and $Ra = 10^5$, the dimensionless cut-line velocity magnitude is 22.2378352103 at Pr = 0.2, 30.2836881514 at Pr = 0.71, and 24.8932028613 at Pr = 10. The response is therefore non-monotonic over the investigated range, and the net change from Pr = 0.2 to 10 is 11.94%. This controlled comparison avoids mixing different block positions.

7.2. Effects on isotherms (Case I)

Figure 8 presents the isotherm patterns at $Ra = 10^5$ for the three Prandtl numbers. At Pr = 0.2, the widely spaced isotherms indicate a thick thermal boundary layer and a conduction-dominated regime, consistent with the high thermal diffusivity that rapidly smooths temperature gradients throughout the domain. As Pr increases to 10, the isotherms crowd sharply near the heated walls and the block surface, signifying a thinning thermal boundary layer and a shift of the dominant transport mechanism from conduction to convection.

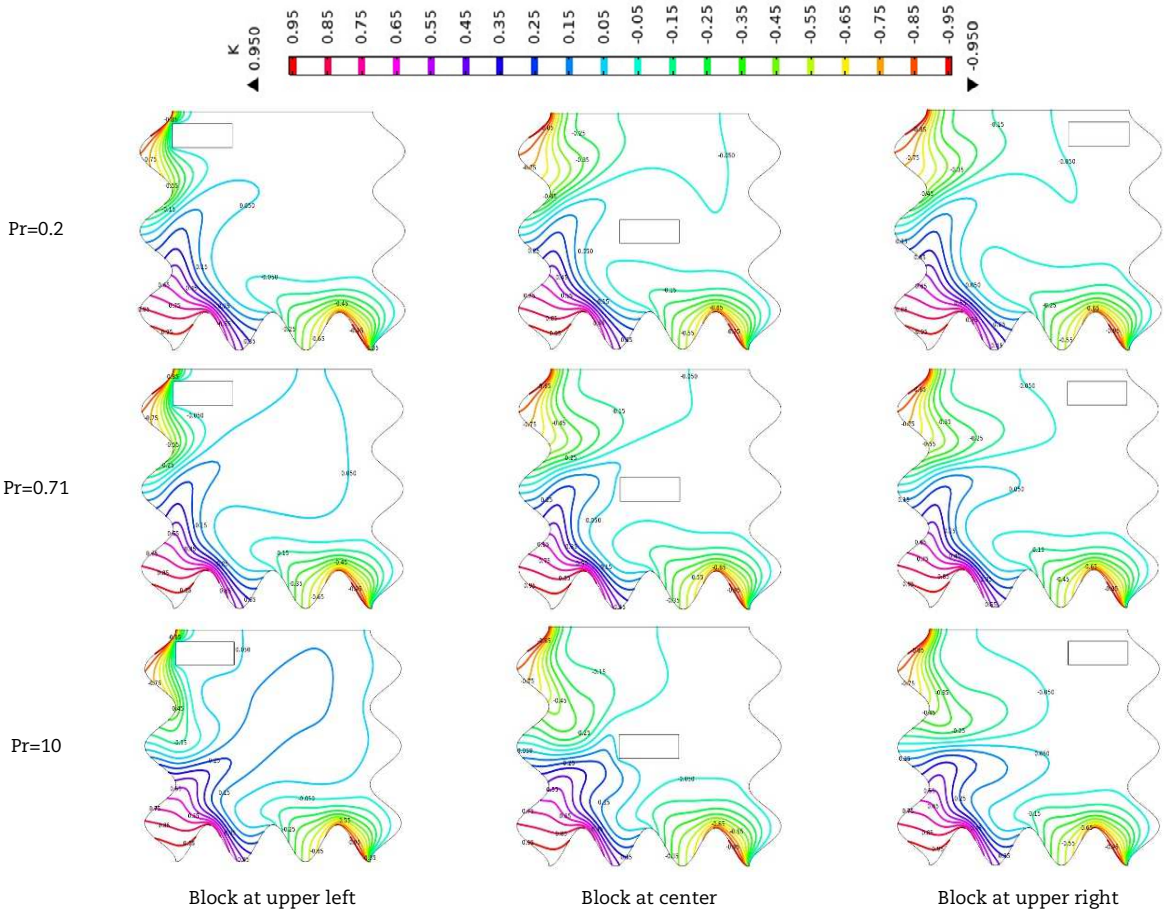


Fig. 8. Effects of Pr for different block positions on isotherms (Case I, dimensionless temperature) when $Ra = 10^5$.

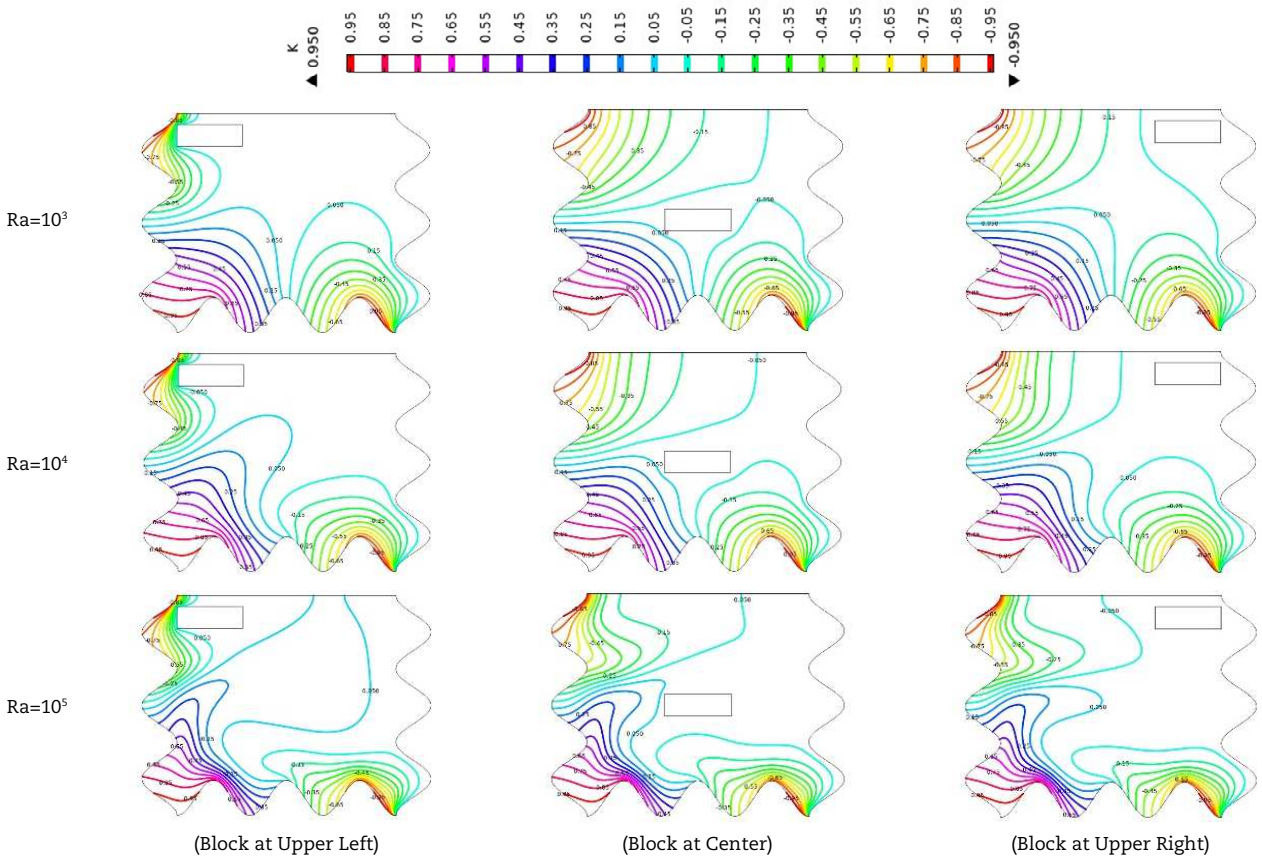


Fig. 9. Effects of Ra for different block positions on isotherms (Case I, dimensionless temperature) when Pr = 0.71.

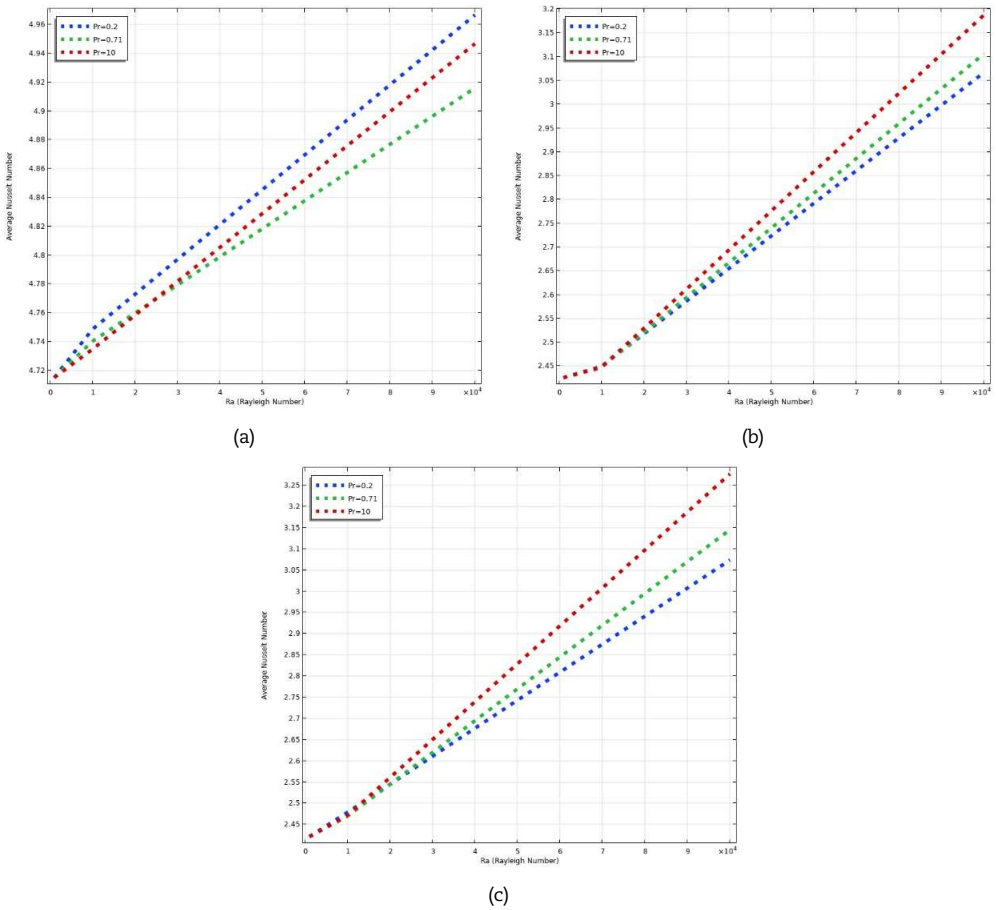


Fig. 10. Relationship between Ra and Nu_{avg} for various Pr when block is at, (a) Upper Left, (b) Center, (c) Upper Right.

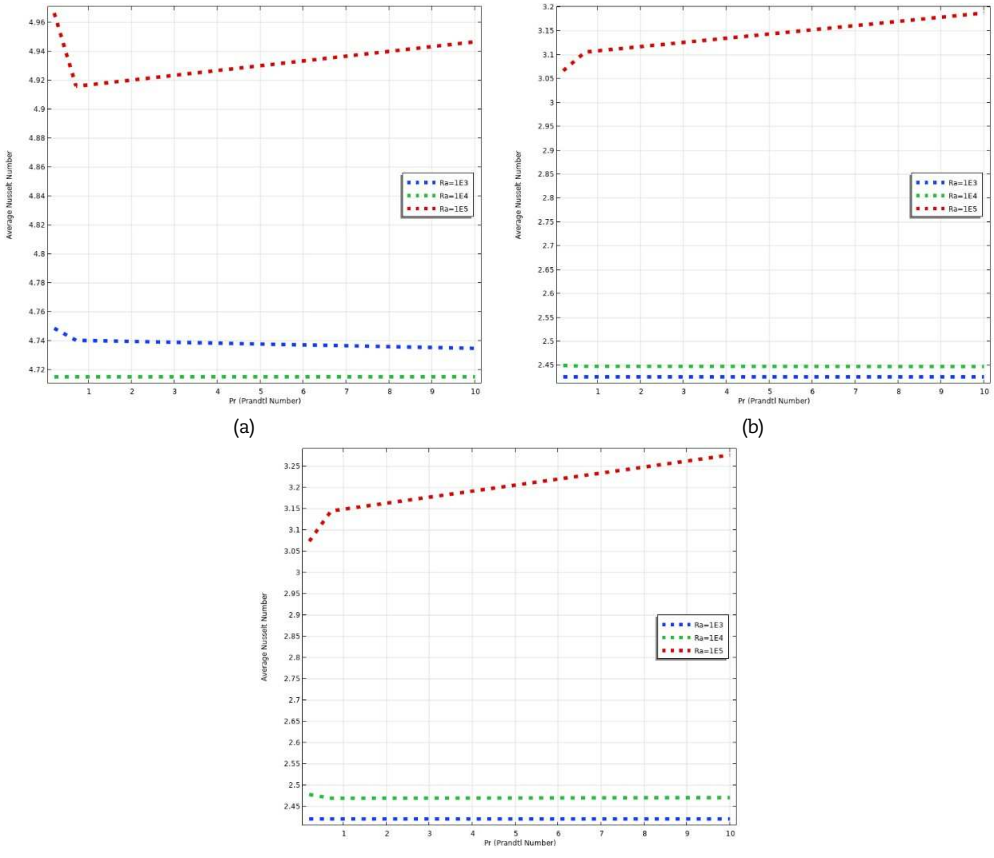


Fig. 11. Relationship between Pr and Nu_{avg} for various Ra when block is at, (a) Upper Left, (b) Center, (c) Upper Right.

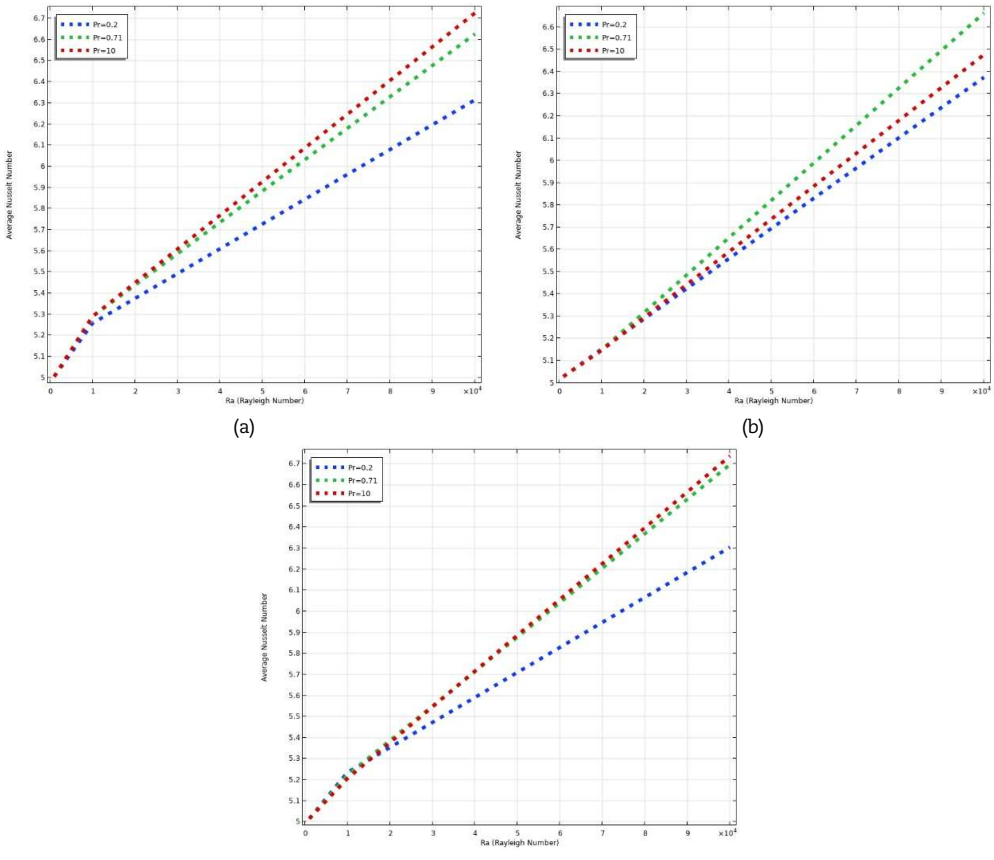


Fig. 12. Relationship between Ra and Nu_{avg} for various Pr when block is at, (a) Upper Left, (b) Center, (c) Upper Right.

The progressive compaction of the isotherms with increasing Pr is therefore interpreted only for those configurations in which the corresponding Nusselt-number curves rise. It is not a universal Prandtl-number effect: depending on block position, plume redirection and block-induced recirculation can weaken or reverse the wall-normal temperature-gradient response, as discussed in Setion 7.3.

Figure 9 isolates the effect of Ra at fixed Pr = 0.71. At Ra = 10^3, the isotherms remain smooth and widely spaced, reflecting a flow field too weak to meaningfully distort the conduction-dominated temperature field. As Ra increases to 10^4 and 10^5, the isotherms become increasingly bent and compressed near the active walls, mirroring the thinning of the thermal boundary layer identified in Section 7.1. The increasing distortion of the isotherms at higher Ra is a direct visual signature of intensifying convective transport overtaking conduction as the dominant heat-transfer mechanism.

7.3. Effects on Nusselt number on different walls (Case I)

Figures 10(a)-10(c) present Nu_{avg} as a function of Ra for the three block positions. For the center and upper-right placements, Nu_{avg} increases with Ra and shows a positive Pr response over the investigated range at the center and upper-right positions. In these configurations, the altered momentum-to-thermal diffusivity ratio is accompanied by boundary-layer compression and stronger wall-normal gradients. This behavior is not universal: at the upper-left position the Pr response reverses, and lower Pr yields a marginally higher Nu_{avg} (≈ 5% higher than at Pr = 10). The reversal is attributed to the local interaction of the block with the periodic wall forcing: plume deflection and recirculation partially shield the active wall, while the broader thermal spread at lower Pr can maintain a larger wall-normal gradient. Thus, Pr modifies heat transfer through a configuration-dependent coupling with block position and the local flow structure rather than through a single monotonic mechanism.

Figures 11(a)–11(c) present the complementary view of Nu_{avg} versus Pr for fixed Ra. For Ra = 10^3 and 10^4, Nu_{avg} remains essentially insensitive to Pr, since the flow is too weak at these Rayleigh numbers for the diffusivity ratio to meaningfully affect the temperature field. At Ra = 10^5, however, Nu_{avg} becomes more sensitive to Pr, but the direction and magnitude of that sensitivity depend on block location, consistent with the position-dependent behavior in Figs. 10(a)–10(c). This confirms that Ra and Pr act in a coupled rather than universally additive manner.

At the bottom wall (Figs. 12(a)–12(c)), Nu_{avg} is lower at Pr = 0.2 than at higher Pr for the plotted bottom-wall configurations, and this difference becomes more visible as Ra increases. This trend is specific to the bottom-wall response in these cases and should not be generalized to every block position or wall. Figures 13(a)–13(c) further show that Pr sensitivity is weak at Ra = 10^3 and 10^4 and becomes appreciable mainly at Ra = 10^5, where stronger circulation makes the local thermal boundary layer more responsive to block placement.

7.4. Effects on velocity magnitude (Case I)

Figures 14(a)–14(c) show that the cut-line velocity increases monotonically with Ra for all Pr, confirming that buoyancy strength is the primary driver of flow intensity, while at a fixed Ra, velocities are consistently higher at Pr = 0.71 than at Pr = 0.2, reflecting the more efficient momentum transport at the intermediate diffusivity ratio.

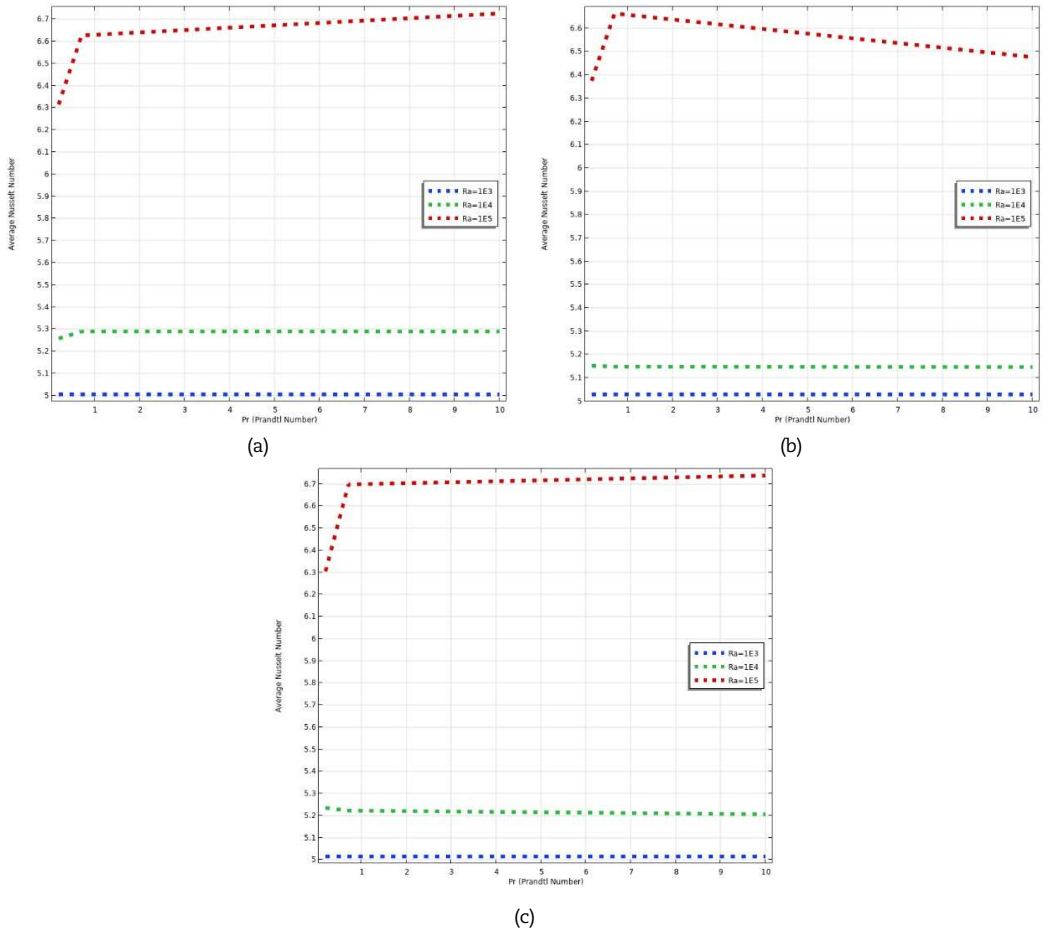


Fig. 13. Relationship between Pr and Nu_{avg} for various Ra when block is at, (a) Upper Left, (b) Center, (c) Upper Right.

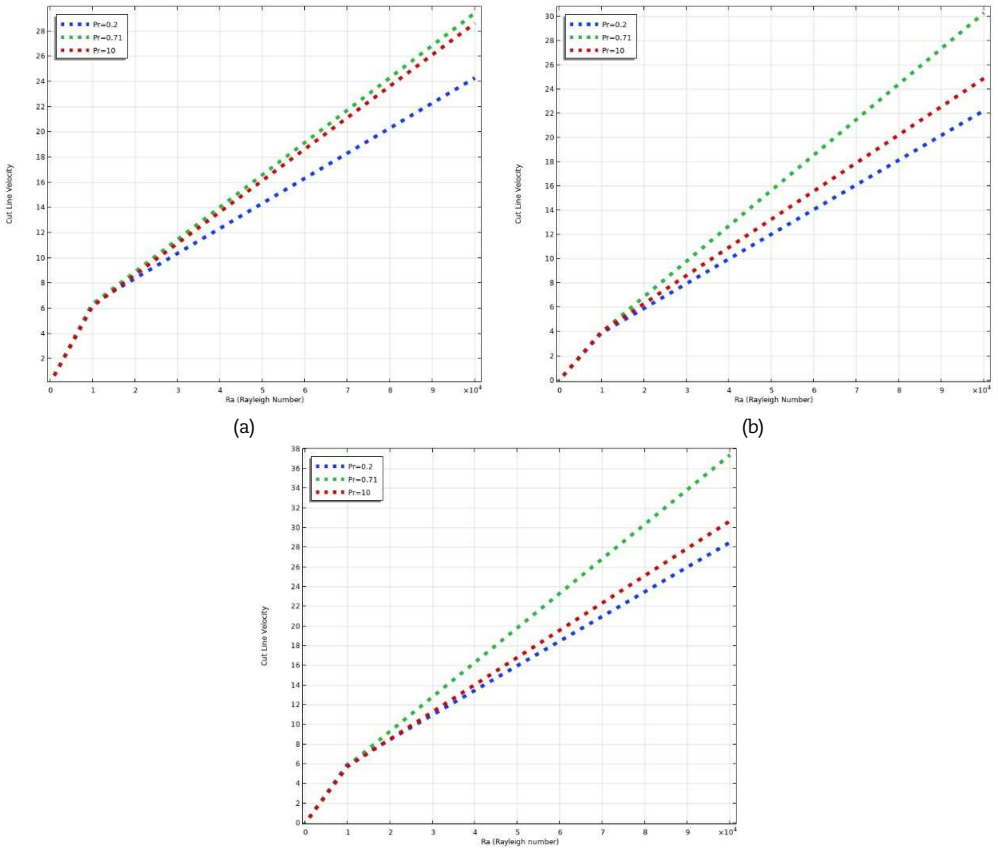


Fig. 14. Relationship between Ra and Velocity for various Pr when block is at, (a) Upper Left, (b) Center, (c) Upper Right.

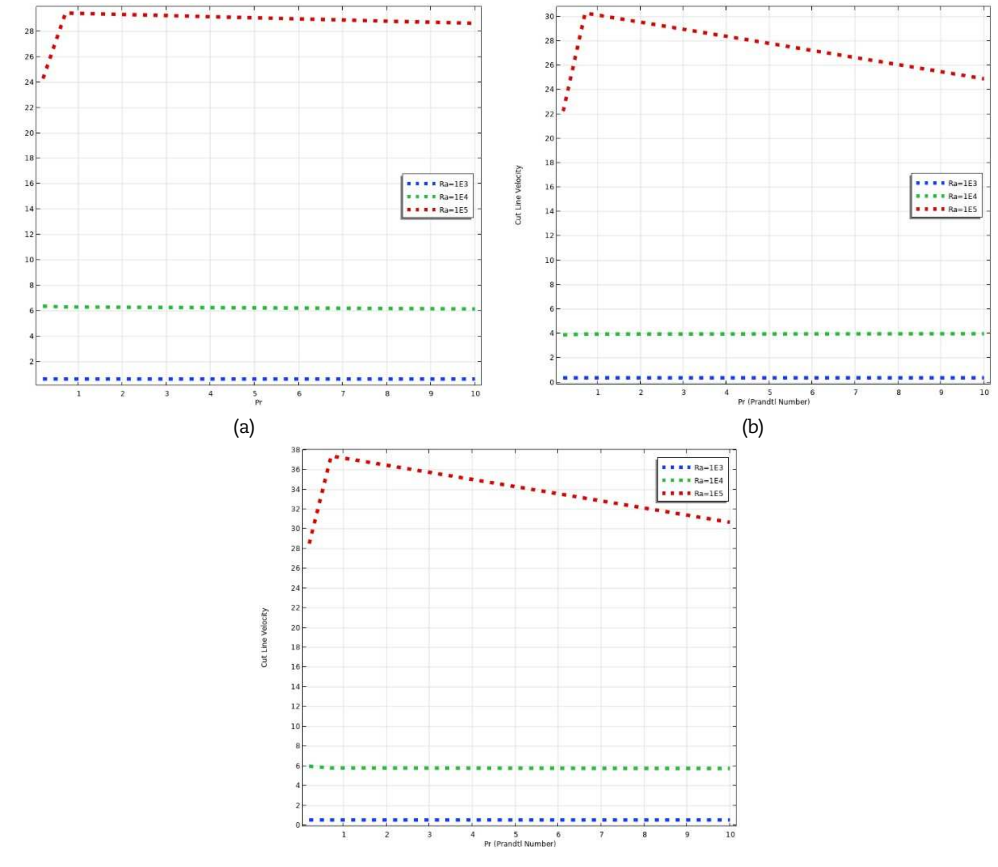


Fig. 15. Relationship between Pr and Velocity for various Ra when block is at, (a) Upper Left, (b) Center, (c) Upper Right.

Figures 15(a)–15(c) show that the cut-line velocity remains nearly invariant with Pr at Ra = 10^3 and 10^4, since the buoyancy forcing at these Rayleigh numbers is too weak to translate diffusivity differences into a measurable velocity response; at Ra = 10^5, the velocity rises sharply at low Pr before gradually declining as Pr increases further, indicating that beyond a certain momentum-to-thermal diffusivity ratio, the increasingly confined shear layers begin to throttle the bulk flow even as local heat transfer continues to intensify.

7.5. Effects on streamlines (Case II)

Figure 16 depicts the Ra-dependence of the flow field when the block acts as an internal heat source. Increasing Ra strengthens the buoyant circulation and produces multiple interacting vortices as the block-generated plume couples with the wall-driven flow. Because all solid boundaries are no-slip, the global minimum velocity magnitude is zero; nonzero lower values shown by a cut line or plotted colour scale should not be interpreted as the domain-wide minimum. At the center position and Pr = 0.71, the dimensionless cut-line velocity magnitude increases from 0.8110253453 at Ra = 10^3 to 34.9648501768 at Ra = 10^5, corresponding to a 4211.19% increase. This same-position comparison replaces the previous 4500% statement and does not imply that Case II has a larger relative increase than Case I.

Figure 17 shows the corresponding Pr-dependence at Ra = 10^5. As Pr increases, the flow transitions from large, smooth, diffusive vortices toward smaller, more intense and spatially concentrated ones, mirroring the boundary-layer-thinning mechanism identified in Case I but here superimposed on a stronger baseline circulation driven by the heated obstruction.

7.6. Effects on isotherms (Case II)

Figure 18 presents isotherms at Ra = 10^5 for the three Prandtl numbers, with the non-dimensional temperature θ spanning –0.950 to 0.950. At Pr = 0.2, the widely spread contours indicate a thick thermal boundary layer and conduction-dominated transport, consistent with the high thermal diffusivity relative to momentum diffusivity. At Pr = 0.71, the isotherms are visibly more compact, indicating a transitional regime combining conduction and convection.

At Pr = 10, the isotherms concentrate sharply around the block and heated walls, signifying a thin thermal boundary layer and strongly convection-dominated transport. Figure 19 further shows that increasing Ra at fixed Pr = 0.71 drives the same qualitative transition from smooth, conduction-like contours at Ra = 10^3 to highly distorted, convection-dominated contours at Ra = 10^5 confirming that both Ra and Pr act through the common physical mechanism of thermal boundary-layer thinning, irrespective of whether the block acts as a heat sink or a heat source.

7.7. Effects on Nusselt number on different walls (Case II)

Figures 20(a)–20(c) show that Nu_{avg} at the left wall increases non-linearly with Ra for all Pr and block positions, with the rate of increase becoming more pronounced at higher Ra, which reflects the self-reinforcing feedback between the heated block's buoyant plume and the wall-driven circulation. Figures 21(a)–21(c) confirm that this Ra-sensitivity is itself conditional on Pr, with Ra = 10^5 producing the most pronounced response while Ra = 10^3 remains nearly flat, consistent with the pattern established in Case I.

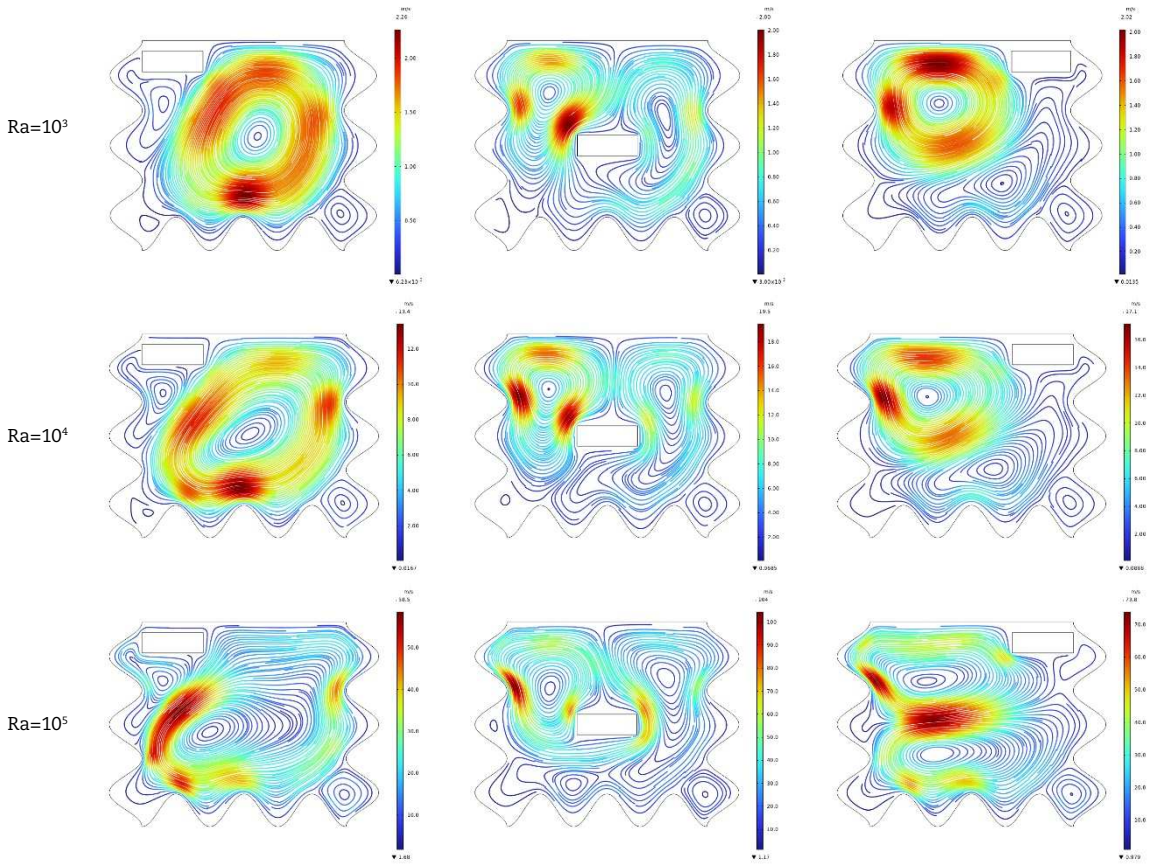


Fig. 16. Effects of Ra for different block positions on streamlines (Case II, dimensionless velocity magnitude) when Pr = 0.71.

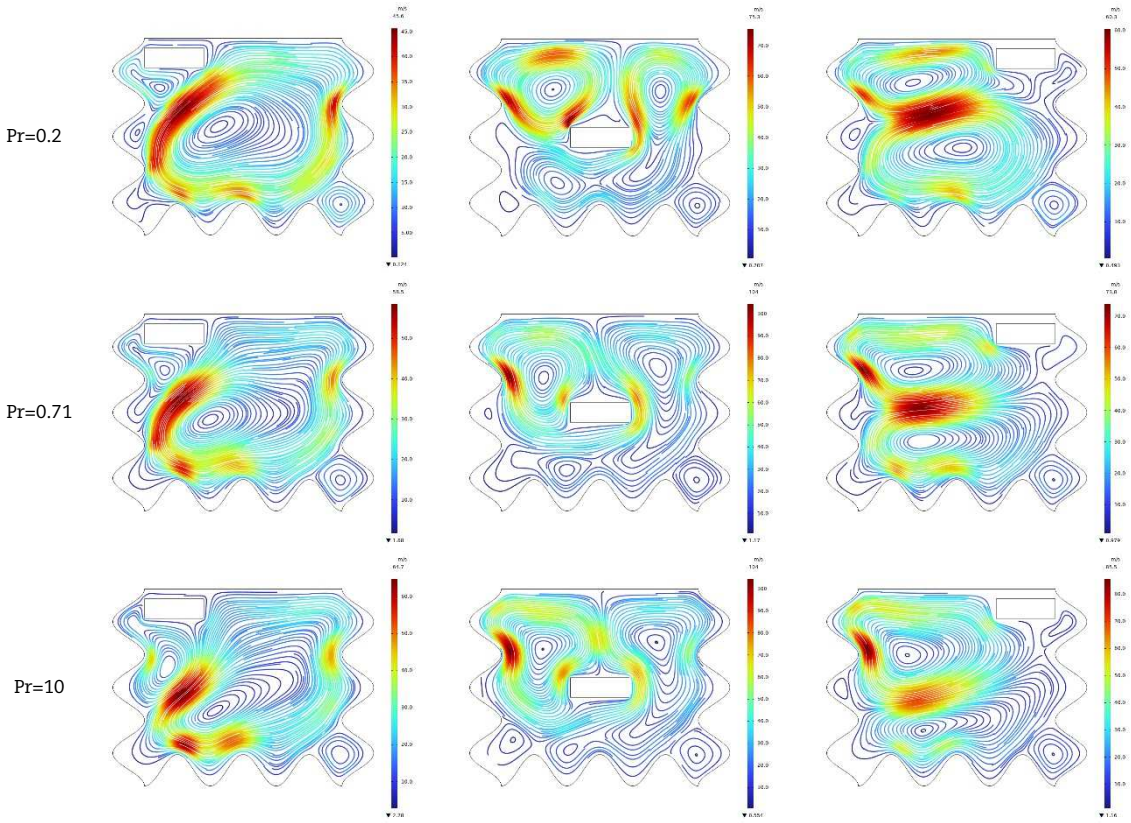


Fig. 17. Effects of Pr for different block positions on streamlines (Case II, dimensionless velocity magnitude) when Ra = 10^5.

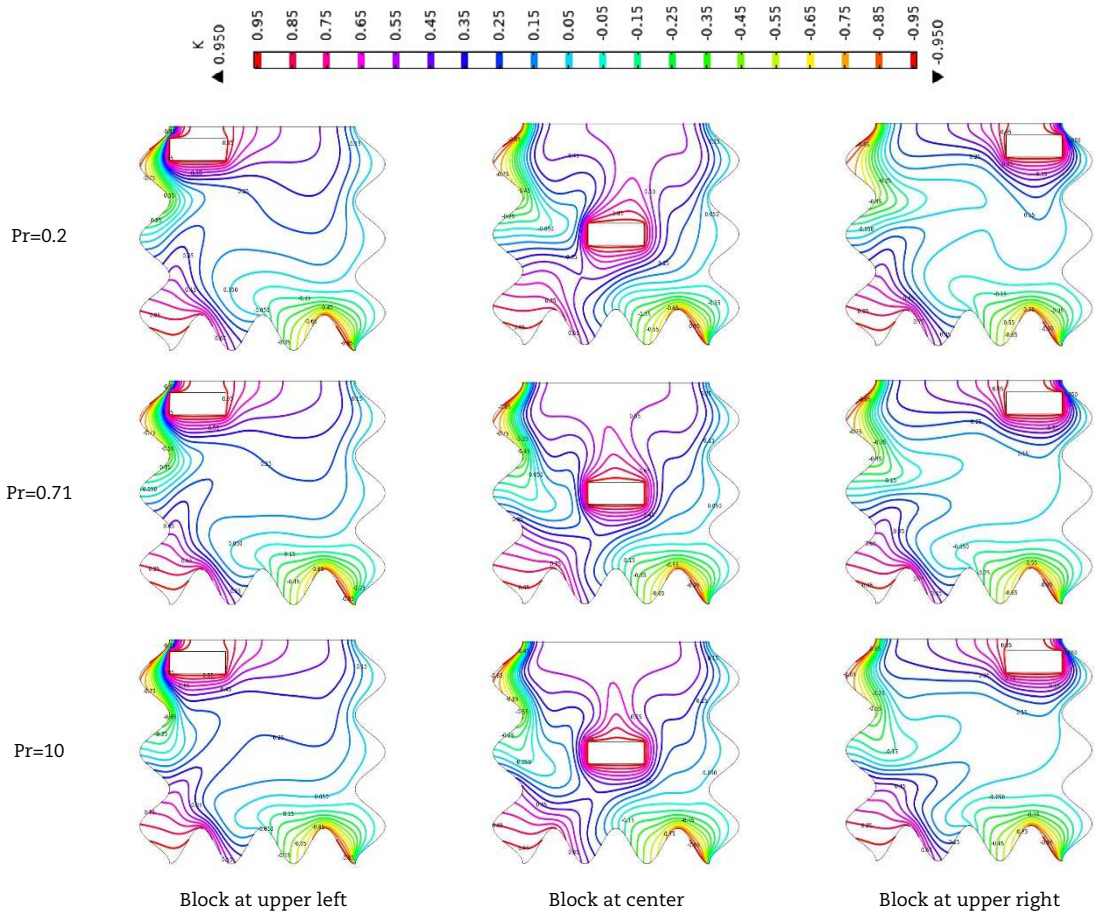


Fig. 18. Effects of Pr for different block positions on isotherms (Case II, dimensionless temperature) when Ra = 10^5.

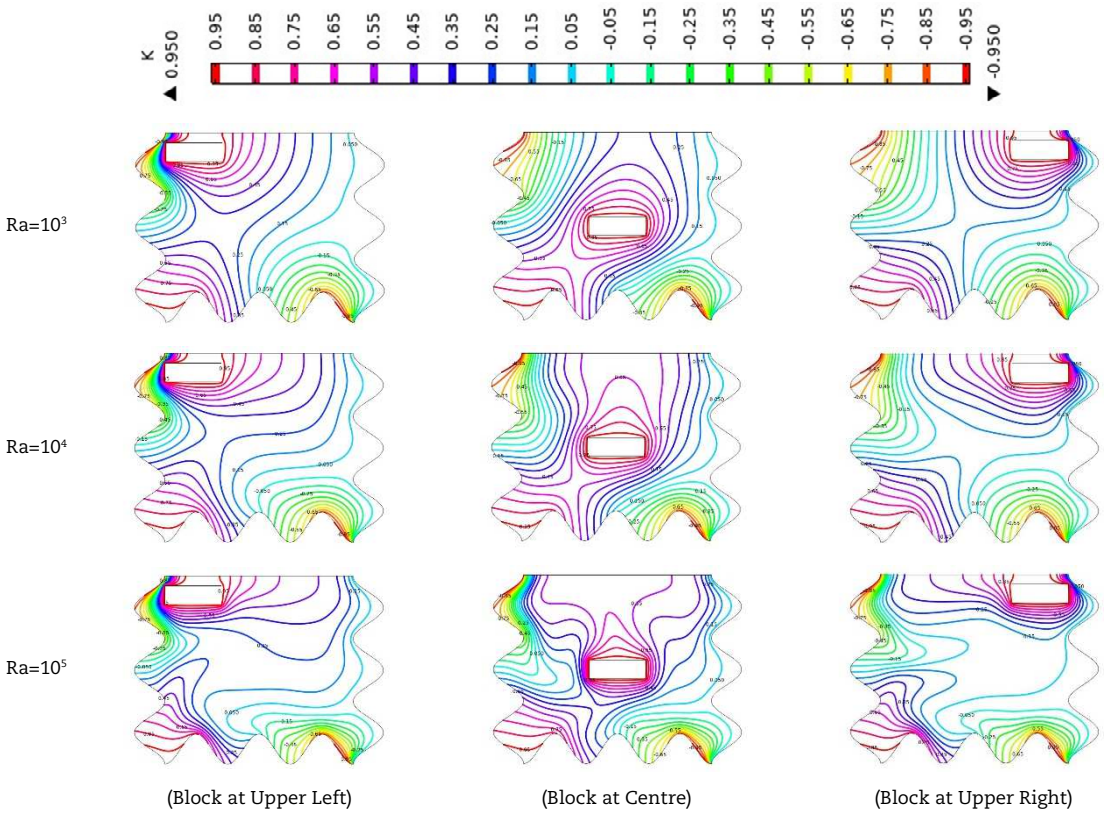


Fig. 19. Effects of Ra for different block positions on isotherms (Case II, dimensionless temperature) when Pr = 0.71.

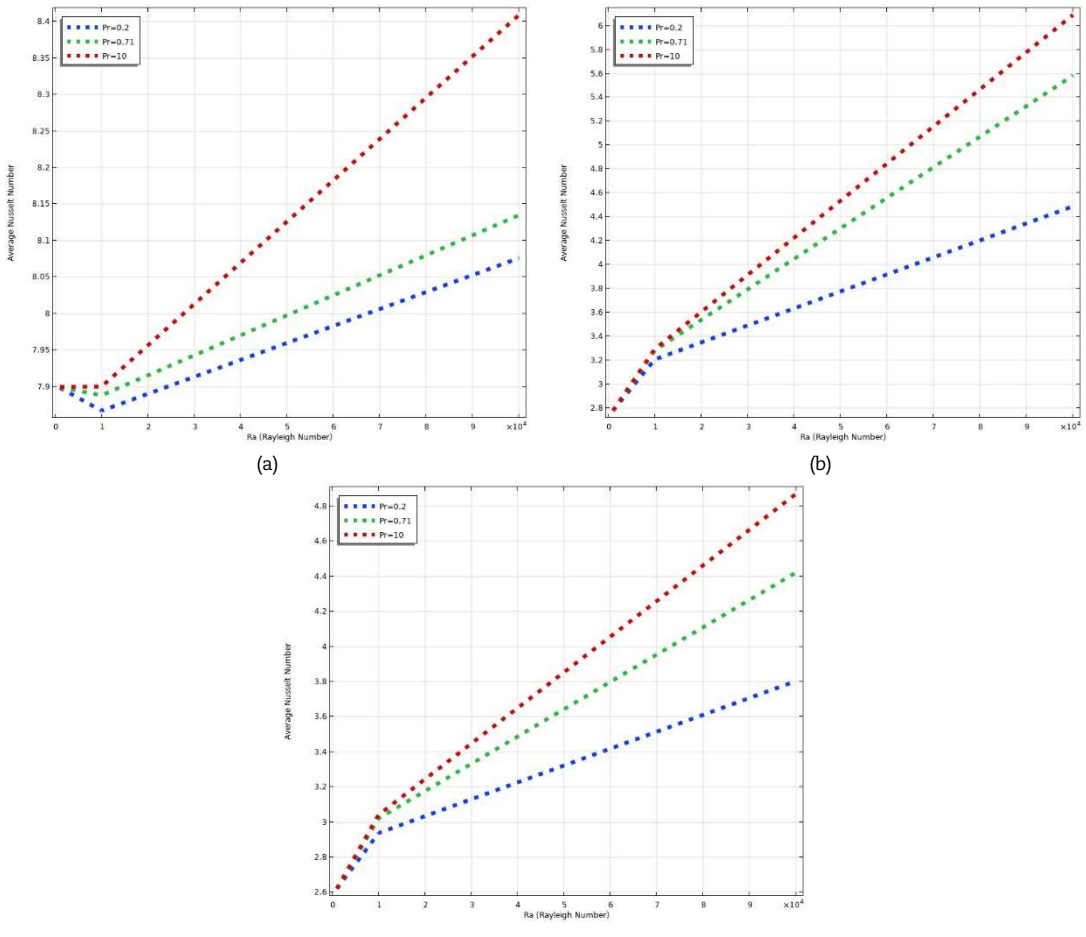


Fig. 20. Relationship between Ra and Nu_{avg} for various Pr when block is at, (a) Upper Left, (b) Center, (c) Upper Right.

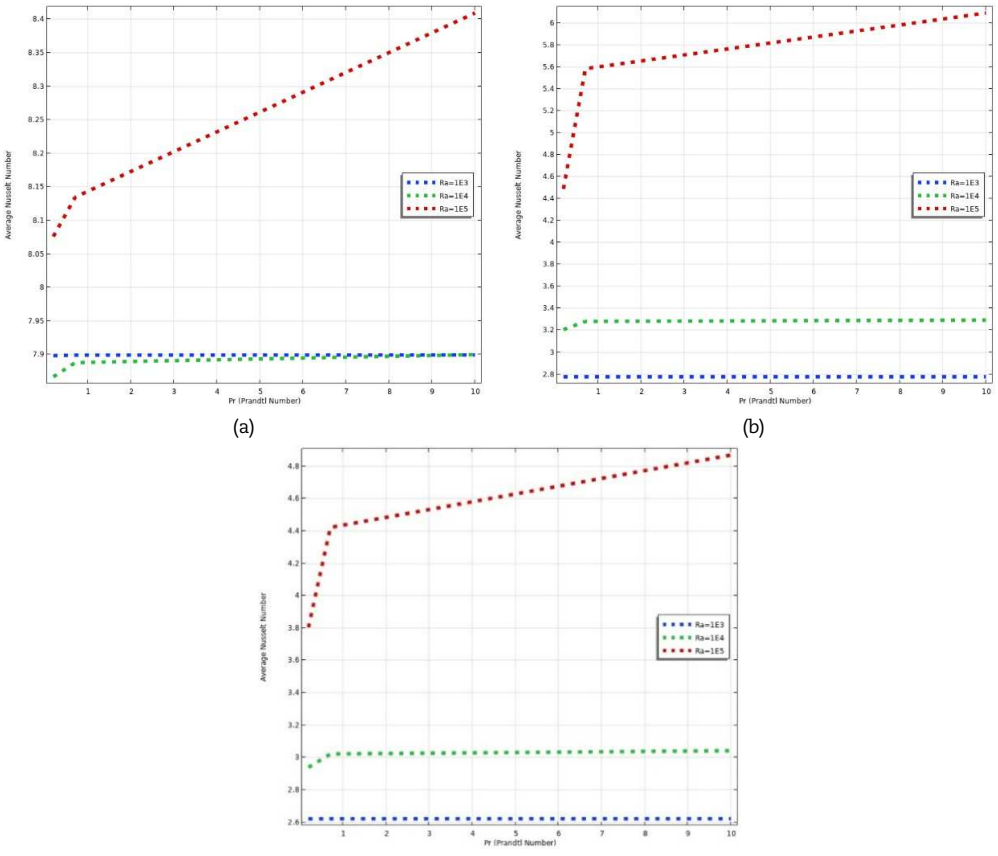


Fig. 21. Relationship between Pr and Nu_{avg} for various Ra when block is at, (a) Upper Left, (b) Center, (c) Upper Right.

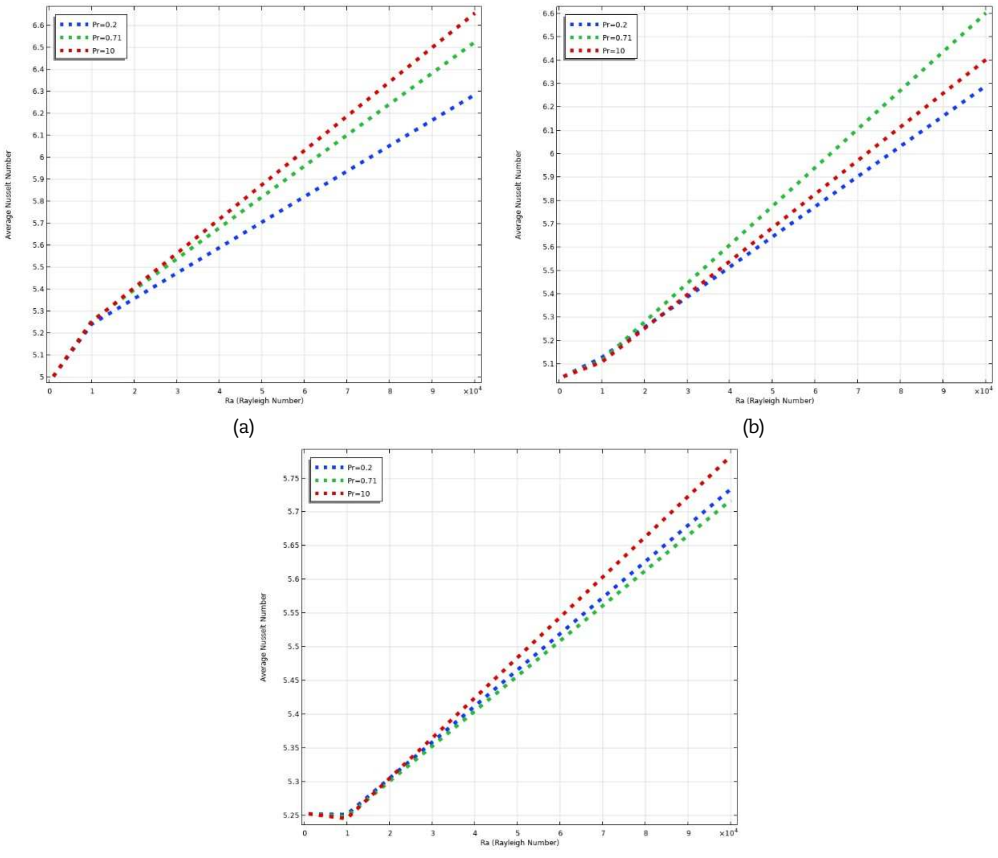


Fig. 22. Relationship between Ra and Nu_{avg} for various Pr when block is at, (a) Upper Left, (b) Center, (c) Upper Right.

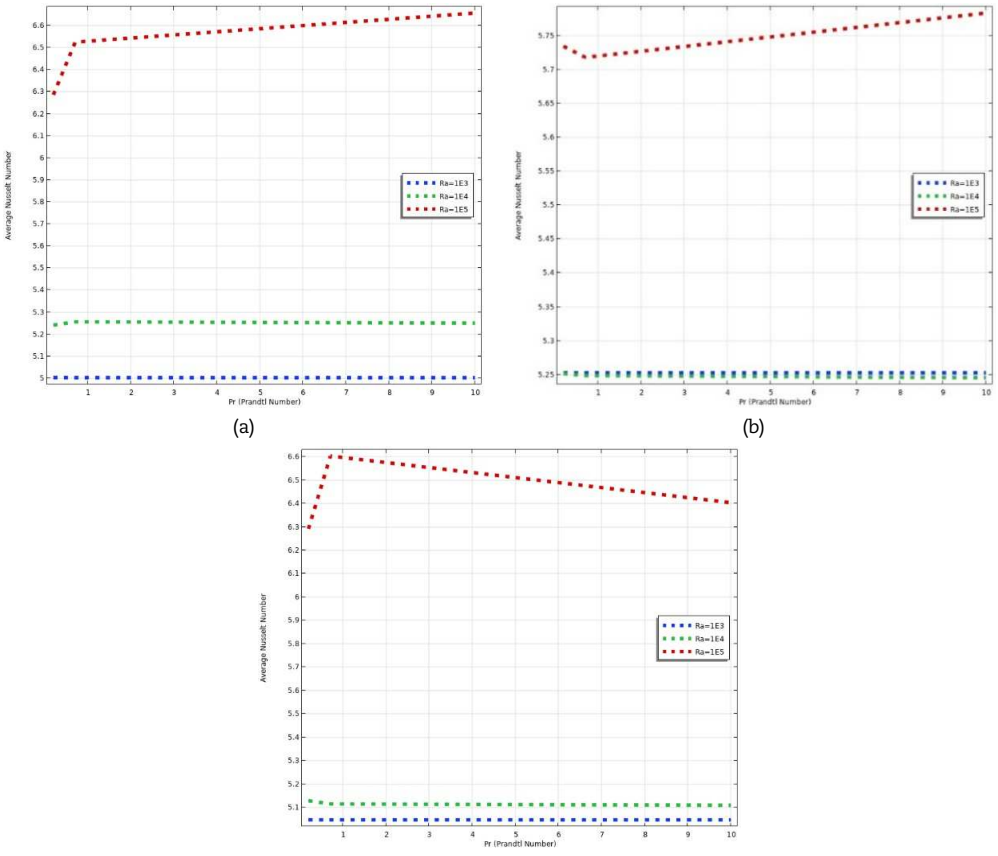


Fig. 23. Relationship between Pr and Nu_{avg} for various Ra when block is at, (a) Upper Left, (b) Center, (c) Upper Right.

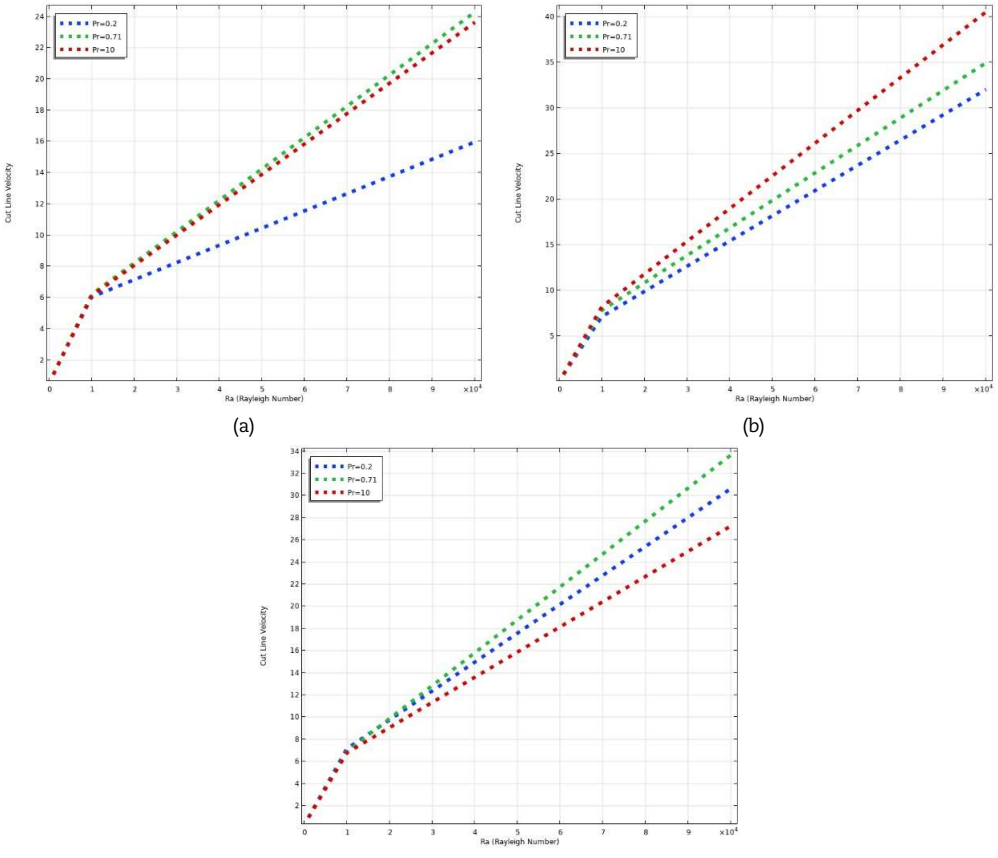


Fig. 24. Relationship between Ra and Velocity for various Pr when block is at, (a) Upper Left, (b) Center, (c) Upper Right.

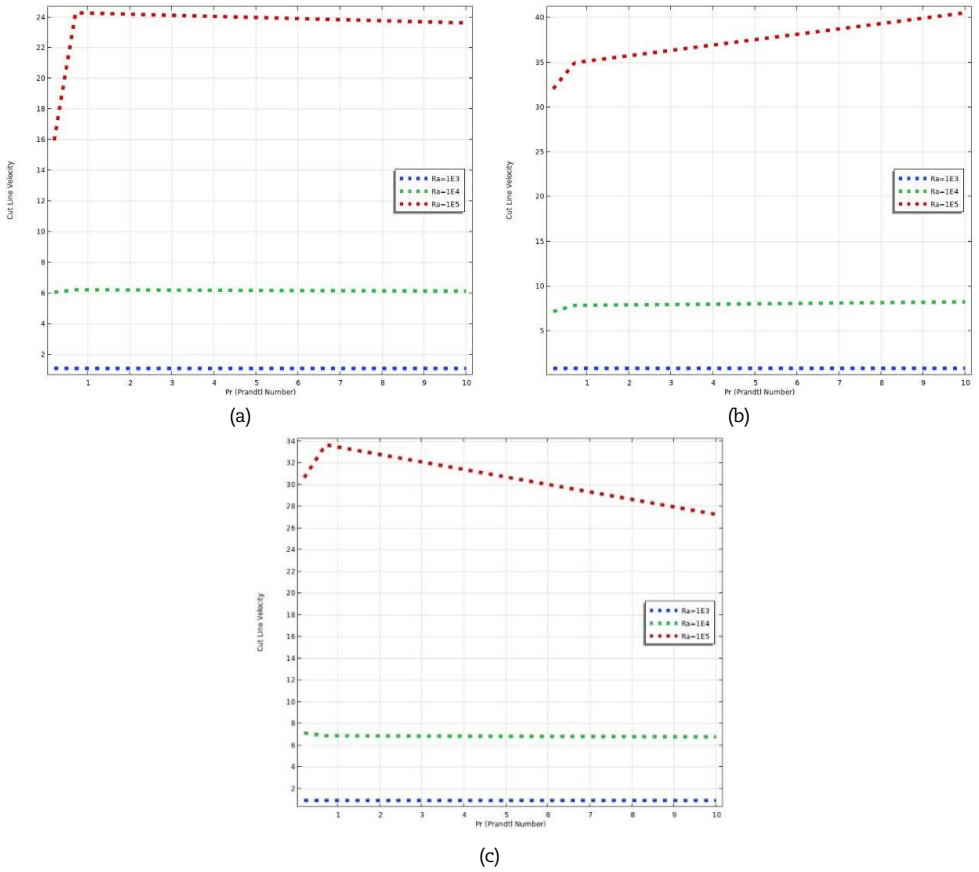


Fig. 25. Relationship between Pr and Velocity for various Ra when block is at, (a) Upper Left, (b) Center, (c) Upper Right.

Taken together with the bottom-wall results (Figs. 22(a)–22(c) and 23(a)–23(c)), the left-wall Nusselt number gain ranges from 6% (upper-left position) to over 110% (center position) as Pr increases from 0.2 to 10, while the bottom wall registers gain of 10–32% depending on block placement. Notably, the upper-left and center positions in Figs. 22(a) and 22(b) show Pr = 10 producing the highest Nu_{avg}, whereas at the upper-right position in Fig. 22(c) the trend inverts, with Pr = 0.71 yielding the highest value which confirms that an echo of the position-dependent reversal already identified in Case I, and further evidence that the interaction between block location and the periodic wavy-wall heating profile, rather than Pr alone, dictates the direction of the Prandtl-number effect at specific positions. Uniquely among all configurations, the upper-left block position in Case II shows a mild decline in Nu_{avg} (≈ 5–6%) with increasing Ra, suggesting that at this position the growing recirculation partially shields the wall from the hottest fluid rather than enhancing near-wall transport. This position-dependent reversal is consistent with plume deflection and block-induced recirculation: depending on placement, the block can either compress the near-wall thermal boundary layer or partially shield the wall from direct fluid renewal.

Table 7 compares the cold- and heated-block cases at Ra = 10^4, fixed Pr, and the same bottom-wavy-wall evaluation. The upper-left and center comparisons use identical block coordinates in both thermal cases. At these coordinate-matched positions, heating the block increases Nu_{avg} at the center by 1.93–1.96%, whereas the upper-left change is only –0.31% to –0.74% and is therefore treated as marginal. The reported upper-right values differ by –1.87% to –2.06%; however, because the saved upper-right coordinates are case-specific (Table 1), this pair is interpreted as a comparison of the two reported upper-right configurations rather than as a strict one-factor thermal-state change. All percentage changes in Tables 7 to 9 were rechecked directly from the original numerical values using $\Delta(\%) = \frac{Nu_2 - Nu_1}{Nu_1} \times 100$ and are reported to two decimal places. Differences with $|\Delta| < 1\%$ are interpreted as marginal and are not used as evidence of a substantive enhancement or deterioration. The streamline and isotherm fields in Figs. 6–9 and 16–19 show that changing the block thermal state reorganizes plume paths and recirculation, thereby modifying the wall-normal thermal gradient that governs Nu_{avg}.

With the block thermal condition fixed as heated, Table 8 isolates the effect of block position on bottom-wall heat transfer. The upper-right placement is consistently the least favorable: moving from the upper-left to the upper-right reduces Nu_{avg} by 2.15–2.70%, whereas moving from the upper-right to the center restores 2.40–2.68%. By contrast, the upper-left and center values differ by only –0.15% to +0.20%, indicating practically equivalent heat-transfer performance at these two positions over the investigated Pr range. The Case-II streamline and isotherm fields in Figs. 16–19 support this result, showing that block relocation changes plume deflection and the coupling between the block-induced buoyant flow and the periodically heated bottom wall, and hence the wall-normal heat-transfer response.

Table 9 provides the corresponding positional comparison for the cold-block condition. A robust ordering is maintained for all investigated Pr values: upper-left > upper-right > center. Moving from the upper-left to the upper-right lowers Nu_{avg} by 0.43–1.58%; shifting from the upper-right to the center produces a further 1.15–1.59% reduction; and the full upper-left-to-center change reaches 2.01–2.71%. Unlike the heated case, where the upper-left and center positions are nearly equivalent, the cold block produces a clear location hierarchy. The Case-I flow and thermal fields in Figs. 6–9 show that the cold obstruction redirects the buoyant circulation and cooled return flow, altering thermal-boundary-layer renewal along the bottom wavy wall and therefore the average wall-normal heat-transfer response.

Table 7. Comparison of cold- and heated-block bottom-wavy-wall Nu_{avg} at Ra = 10^4 for the three reported block-location categories.

Pr	Upper left			Center			Upper right		
	Cold block Nu_{avg}	Heated block Nu_{avg}	Change (%)	Cold block Nu_{avg}	Heated block Nu_{avg}	Change (%)	Cold block Nu_{avg}	Heated block Nu_{avg}	Change (%)
0.2	5.2575	5.2412	-0.31	5.1516	5.2515	+1.94	5.2348	5.1283	-2.03
0.71	5.2896	5.2562	-0.63	5.1477	5.2485	+1.96	5.2224	5.1147	-2.06
10	5.2894	5.2503	-0.74	5.1460	5.2454	+1.93	5.2060	5.1087	-1.87

Table 8. Pairwise effect of block position on bottom-wavy-wall Nu_{avg} for the heated-block condition (Case II) at Ra = 10^4.

Pr	Upper left → Upper right			Upper right → Center			Upper left → Center		
	Upper left	Upper right	Change (%)	Upper right	Center	Change (%)	Upper left	Center	Change (%)
0.2	5.2412	5.1283	-2.15	5.1283	5.2515	+2.40	5.2412	5.2515	+0.20
0.71	5.2562	5.1147	-2.69	5.1147	5.2485	+2.62	5.2562	5.2485	-0.15
10	5.2503	5.1087	-2.70	5.1087	5.2454	+2.68	5.2503	5.2454	-0.09

Table 9. Pairwise effect of block position on bottom-wavy-wall Nu_{avg} for the cold-block condition (Case I) at Ra = 10^4.

Pr	Upper left → Upper right			Upper right → Center			Upper left → Center		
	Upper left	Upper right	Change (%)	Upper right	Center	Change (%)	Upper left	Center	Change (%)
0.2	5.2575	5.2348	-0.43	5.2348	5.1516	-1.59	5.2575	5.1516	-2.01
0.71	5.2896	5.2224	-1.27	5.2224	5.1477	-1.43	5.2896	5.1477	-2.68
10	5.2894	5.2060	-1.58	5.2060	5.1460	-1.15	5.2894	5.1460	-2.71

Collectively, Tables 7–9 establish that neither block heating/cooling nor block position has a universal effect on heat transfer. Their influences are strongly coupled: the same change in block thermal state can enhance or suppress Nu_{avg} depending on position, while the preferred position changes between heated- and cold-block conditions. This controlled same-wall comparison therefore provides a clearer design basis for selecting internal-component placement according to the intended thermal-management objective.

The broader recent FEM literature [32–35] likewise shows that complex boundaries and internal thermal features can strongly reorganize transport. Direct numerical comparison with those studies is not appropriate here, however, because they include additional NEPCM, porous-medium, magnetic, radiative, phase-change, mixed-convection, or data-driven physics that are absent from the present single-fluid natural-convection model.

7.8. Effects on velocity magnitude (Case II)

Figures 24(a)–24(c) confirm that the cut-line velocity magnitude increases with Ra across all Pr values, consistent with intensifying buoyant circulation reinforced by the heated block. Figures 25(a)–25(c) show that this velocity remains essentially constant at Ra = 10^3 and 10^4 where the flow is too weak for diffusivity effects to register but rises sharply and becomes strongly Pr-dependent at Ra = 10^5, mirroring the coupled Ra–Pr sensitivity already established for the Nusselt number. This consistent parallel between the velocity and heat-transfer responses across both thermal configurations reinforces the central physical conclusion of this study. Buoyancy strength (Ra) sets the overall intensity of the convective response, while the momentum-to-thermal diffusivity ratio (Pr) governs how that response is spatially distributed in broad and diffuse at low Pr, sharply localized at high Pr with the block's thermal condition (heat sink or heat source) and position further modulating both the magnitude and, in specific instances, the direction of these trends. At the center position and Ra = 10^5, the Case-II dimensionless cut-line velocity changes from 32.0420 at Pr = 0.2 to 40.536 at Pr = 10, a controlled increase of 26.51%.

8. Conclusion

This study numerically investigated steady, laminar natural convection in a wavy square cavity containing a rectangular block, using the finite element Galerkin method in COMSOL Multiphysics, under two thermally contrasting scenarios: a cold block (Case I, heat sink) and a heated block (Case II, heat source) across three block positions and $10^3 \le Ra \le 10^5$, Pr = 0.2, 0.71, 10. Across both cases, buoyancy strength (Ra) and the relative dominance of momentum over thermal diffusivity (Pr) jointly governed the transition from a conduction-dominated, single-vortex flow to a convection-dominated, multi-cellular regime.

The key outputs of the study are summarized below:

- Case I (cold block): At the center position and Pr = 0.71, the dimensionless cut-line velocity magnitude increases from 0.3687 at Ra = 10^3 to 30.2837 at Ra = 10^5 (8112.73%). The Nusselt-number response remains position dependent, including the upper-left reversal discussed in Section 7.3.
- Case II (heated block): At the center position and Pr = 0.71, the dimensionless cut-line velocity magnitude increases from 0.8110 at Ra = 10^3 to 34.9649 at Ra = 10^5 (4211.19%). The heated-block results are interpreted separately from Case I except for the controlled same-wall, same-position thermal-state comparison reported in Table 7.
- Physical mechanism: Higher Ra generally thins the thermal boundary layer and steepens near-wall gradients. The influence of Pr is position dependent and can be non-monotonic because momentum and thermal diffusion interact with plume redirection, recirculation, and the local wall-normal temperature gradient.
- Block position: Center/upper-right placements split the buoyant plume into multiple cells, amplifying Pr-sensitivity; upper-left placement preserved a stable single-vortex pattern with weak or inverse Pr-sensitivity.

Design implication: For a strict thermal-state comparison, the block coordinates and wall conditions must be matched. In Table 7 this condition is satisfied at the upper-left and center positions; the reported upper-right values use the case-specific coordinates listed in Table 1 and are therefore interpreted only as a comparison of the two upper-right configurations. Under the matched comparisons, heating the block enhances bottom-wall heat transfer at the center while producing only a marginal reduction at the upper-left, so block thermal state and placement must be selected jointly for the intended thermal-management objective.



Design insights and limitations: The parametric results provide the following design-oriented observations within the investigated two-dimensional steady laminar model:

- Rayleigh number: increasing Ra strengthens buoyancy-driven circulation and compresses the thermal boundary layer; the present conclusions are limited to $10^3 \leq Ra \leq 10^5$ and should not be extrapolated to transitional or turbulent regimes.
- Prandtl number: the Pr response is coupled to Ra and block position rather than universally monotonic; in particular, the upper-left placement can exhibit an inverse or weak sensitivity because plume redirection and recirculation modify the local wall-normal temperature gradient.
- Block thermal condition: At Ra = 10^4 on the bottom wavy wall, changing the block from cold to heated at the coordinate-matched center position increases Nu_{avg} by 1.93-1.96%, while the coordinate-matched upper-left change is marginal (-0.31% to -0.74%). The case-specific upper-right configurations differ by -1.87% to -2.06%, but because their saved x-coordinates differ between Cases I and II (Table 1), that difference is not interpreted as a pure thermal-state effect.
- Block position: Under the heated-block condition at Ra = 10^4, the upper-left and center positions remain nearly equivalent (within ±0.20%), whereas the upper-right position is consistently lower. Under the cold-block condition, the bottom-wall Nu_{avg} follows upper-left > upper-right > center for all investigated Pr values, with a 2.01-2.71% decrease from upper-left to center.
- Future work should examine pointwise local-Nusselt distributions, transient and three-dimensional regimes, broader geometric parameters, and common normalized performance measures for comparing different imposed thermal loads.

Author Contributions

The contribution of authors are as follows: Md.S. Rahman - Formal analysis, Investigation, Visualization, Software, Writing-review and editing; M.A. Mishu - Formal analysis, Investigation, Methodology, Visualization, Software; Md.A. Hossain - Conceptualization, Investigation, Methodology, Software, Writing-original draft, Writing-review and editing, Supervision; Md.A. Rahman - Validation, Investigation, Methodology, Writing-review and editing; G.M. Zahidul Islam - Formal analysis, Investigation, Visualization, Writing-review and editing; Md.R. Hossain - Formal analysis, Validation, Writing-original draft, Software; A. Mehejabin - Formal analysis, Investigation, Visualization, Writing-review and editing. The manuscript was written through the contribution of all authors. All authors discussed the results, reviewed, and approved the final version of the manuscript.

Acknowledgments

The authors acknowledge the use of AI-assisted language editing tools to improve the clarity and readability of the manuscript. All scientific content and conclusions are the responsibility of the authors. The authors are also grateful to Muhammad Ziaul Haque, PUST for his unconditional and continuous support.

Conflict of Interest

The authors declare that they have no known competing financial interests or personal relationships that could have appeared to influence the work reported in this paper.

Funding

Not applicable.

Data Availability Statements

Data will be made available upon request.

Nomenclature

l	Length of the rectangular block	C_p	Specific heat
H	Height of rectangular block	B_f	Body force
T_h	Heated wall temperature	γ	Ratio of specific heat
T_c	Cold wall temperature	P	Dimensionless pressure
T	Temperature	θ	Dimensionless temperature
u, v	Dimensional velocity components	$\mathrm{Nu_{loc}}$	Local Nusselt number
Pr	Prandtl number	$\mathrm{Nu_{avg}}$	Average Nusselt number
Ra	Rayleigh number	x, y	Dimensional Cartesian coordinates
ρ	Density	X, Y	Dimensionless Cartesian coordinates
α	Thermal diffusivity	U, V	Dimensionless velocity components
μ	Dynamic viscosity	g	Gravitational acceleration
K	Thermal conductivity	n	Outward wall-normal direction

References

[1] Subhani, S., Kumar, R.S., Natural Convection Heat Transfer Enhancement of Circular Obstacle within Square Enclosure, *Journal of Thermal Analysis and Calorimetry*, 147, 2022, 4711-4729.
[2] Khan, Z.H., Hamid, M., Khan, W.A., Ahmad, R., Jie, L., Effects of sinusoidal wall temperature on thermal dynamics and irreversibility around an inclined plate embedded in a square cavity, *Journal of Computational Design and Engineering*, 11(5), 2024, 355-368.
[3] Mohebbi, R., Ma, Y., Soleymani, P., Investigating the Impact of Sinusoidal Walls on Fluid Flow and Heat Transfer Performance of C-Shaped Cavity, *Iranian Journal of Science and Technology, Transactions of Mechanical Engineering*, 49, 225, 349–360.
[4] Khan, Y., Mahmood, R., Majeed, A.H., Irshad, S., Alameer, A., Faraz, N., Finite element simulations of inclined magnetic field and mixed convection in an enclosure with periodically heated walls in the presence of an obstacle, *Frontiers in Physics*, 10, 2022, 1006023.

[5] Khan, Y., Majeed, A.H., Shahzad, H., Awan, F.J., Iqbal, K., Ajmal, M., Faraz, N., Numerical computations of non-Newtonian fluid flow in a hexagonal cavity with an internal obstruction, *Frontiers in Physics*, 10, 2022, 891163.
[6] Fayz-Al-Asad, M., Alam, M.N., Ahmad, H., Sarker, M., Alsulami, M., Gepreel, K.A., Impact of a closed space rectangular heat source on natural convective flow through triangular cavity, *Results in Physics*, 23, 2021, 104011.
[7] Alturaihi, M.H., Jassim, L., ALguboori, A.R., Habeeb, L.J., Jalghaf, H.K., Porosity Influence on Natural Convection Heat Transfer from a Heated Cylinder in a Square Porous Enclosure, *Journal of Mechanical Engineering Research and Developments*, 43(6), 2020, 236-254.
[8] Boulahia, Z., Boulahia, C., Sehaqui, R., Two-phase computation of free convection and entropy generation inside an enclosure filled by a hybrid Al2O3-TiO2-Cu/water nanofluid having a corrugated heat source using the generalized Buongiorno model, *Materials Today: Proceedings*, 30, 2020, 1056-1067.
[9] El Moutaouakil, L., Boukendil, M., Zrikem, Z., Abdelbaki, A., Natural convection and surface radiation heat transfer in a cavity with vertically oriented fins, *Materials Today: Proceedings*, 27, 2020, 3051-3057.
[10] Fayz-Al-Asad, M., Munshi, M., Sarker, M.M.A., Effect of Fin Length and Location on Natural Convection Heat Transfer in a Wavy Cavity, *International Journal of Thermofluid Science and Technology*, 7(3), 2020, 070303.
[11] Gumir, F.J., Al-Farhany, K., Jamshed, W., El-Din, E.S.M.T., Abd-Elmonem, A., Natural convection in a porous cavity filled with (35% MWCNT-65% Fe3O4)/water hybrid nanofluid with a solid wavy wall, *Scientific Reports*, 12, 2022, 17794.
[12] Islam, T., Nur-Alam, M., Asjad, M.I., Parveen, N., Chu, Y., Heatline visualization of MHD natural convection heat transfer of nanofluid in a prismatic enclosure, *Scientific Reports*, 11, 2021, 10972.
[13] Alsabery, A., Kadhim, H., Ismael, M., Hashim, I., Chamkha, A.J., Impacts of amplitude and heat source on natural convection of hybrid nanofluids into a wavy enclosure via heatline approach, *Waves in Random and Complex Media*, 33, 2023, 1060-1084.
[14] Roy, N.C., MHD natural convection of a hybrid nanofluid in an enclosure with multiple heat sources, *Alexandria Engineering Journal*, 61, 2022, 1679-1694.
[15] Giwa, S., Sharifpur, M., Ahmadi, M., Meyer, J., A review of magnetic field influence on natural convection heat transfer performance of nanofluids in square cavities, *Journal of Thermal Analysis and Calorimetry*, 145, 2021, 2581–2623.
[16] Omidpanah, M., Mirjalily, S.A.A., Kargarsharifabad, H., Shoeibi, S., Numerical simulation of combined transient natural convection and volumetric radiation inside hollow bricks, *Journal of Heat and Mass Transfer Research*, 8, 2021, 151-162.
[17] Tayebi, T., Chamkha, A.J., Magnetohydrodynamic natural convection heat transfer of hybrid nanofluid in a square enclosure in the presence of a wavy circular conductive cylinder, *Journal of Thermal Science and Engineering Applications*, 12, 2020, 031009.
[18] Mliki, B., Abbassi, M.A., Entropy generation of MHD natural convection heat transfer in a heated incinerator using hybrid-nanoliquid, *Propulsion and Power Research*, 10, 2021, 143-154.
[19] Tasnim, S., Mitra, A., Saha, H., Islam, M.Q., MHD conjugate natural convection and entropy generation of a nanofluid-filled square enclosure with multiple heat-generating elements in the presence of Joule heating, *Results in Engineering*, 17, 2023, 100993.
[20] Zidan, A.M., Tayebi, T., Dogonchi, A.S., Chamkha, A.J., Ben Hamida, M.B., Galal, A.M., Entropy-based analysis and economic scrutiny of magneto-thermal natural convection enhancement in a nanofluid-filled porous trapezium-shaped cavity having localized baffles, *Waves in Random and Complex Media*, 35, 2025, 7100-7120.
[21] Zheng, Y., Yaghoubi, S., Dezfulizadeh, A., Aghakhani, S., Karimipour, A., Tlili, I., Free convection/radiation and entropy generation analyses for nanofluid of inclined square enclosure with uniform magnetic field, *Journal of Thermal Analysis and Calorimetry*, 141, 2020, 635-648.
[22] Dogonchi, A.S., Tayebi, T., Karimi, N., Chamkha, A.J., Alhumade, H., Thermal-natural convection and entropy production behavior of hybrid nanoliquid flow under the effects of magnetic field through a porous wavy cavity with three circular cylinders, *Journal of the Taiwan Institute of Chemical Engineers*, 124, 2021, 162-173.
[23] Islam, T., Parveen, N., Fayz-Al-Asad, M., Hydromagnetic Natural Convection Heat Transfer of Copper-Water Nanofluid within a Right-Angled Triangular Cavity, *International Journal of Thermofluid Science and Technology*, 7(3), 2020, 070304.
[24] Ganesh, N.V., Al-Mdallal, Q.M., Öztop, H.F., Kalaivanan, R., Analysis of natural convection for a Casson-based multiwall carbon nanotube nanofluid in a partially heated wavy enclosure with a circular obstacle in the presence of thermal radiation, *Journal of Advanced Research*, 39, 2022, 167-185.
[25] Roy, S., Basak, T., Finite element analysis of natural convection flows in a square cavity with non-uniformly heated wall(s), *International Journal of Engineering Science*, 43, 2005, 668-680.
[26] Zienkiewicz, O.C., Taylor, R.L., *The Finite Element Method*, 4th ed., McGraw-Hill, New York, 1991.
[27] Paroncini, M., Corvaro, F., Montucchiari, A., Nardini, G., A numerical and experimental analysis on natural convective heat transfer in a square enclosure with partially active side walls, *Experimental Thermal and Fluid Science*, 36, 2012, 118-125.
[28] Es-Sabry, Y., Chaabelasri, E., Jeyar, M., Benaicha, M., Numerical assessment of meshless method for studying nanofluid natural convection in a corrugated wall square cavity, *International Journal of Renewable Energy Development*, 12(5), 2023, 853-863.
[29] Es-Sabry, Y., Benaicha, M., Ammari, N., Chaabelasri, E., Numerical modeling of buoyancy-driven convection in a porous wavy-walled square cavity under a partially applied magnetic field using a meshless RBF-FD method, *Heat and Mass Transfer*, 62(5), 2026, 50.
[30] Es-Sabry, Y., Benaicha, M., Ammari, N., Chaabelasri, E., Magnetohydrodynamic Natural Convection of Cu-Water Nanofluid in a Tilted Wavy Right-Angled Triangular Cavity: Numerical Study using Meshless RBF-FD Method, *Iranian Journal of Science and Technology, Transactions of Mechanical Engineering*, 2026. https://doi.org/10.1007/s40997-026-00989-0.
[31] Es-Sabry, Y., Benaicha, M., Jeyar, M., Chaabelasri, E., Meshless numerical analysis of natural MHD convection in a zigzag trapezoidal cavity filled with nanofluid, *International Journal of Thermofluids*, 26, 2025, 101041.
[32] Turabi, Y.U.U.B., Xiong, H., Shi, X., Chen, H., Fei, J., Double diffusive heat and mass transfer in a multilayer trapezoidal solar-receiver filled with nano-encapsulated phase change materials, *International Communications in Heat and Mass Transfer*, 175, 2026, 111054.
[33] Turabi, Y.U.U.B., Xiong, H., Chen, W., Fei, J., Shi, X., Ahmad, S., Enhanced thermal energy storage of nano encapsulated phase change material filled porous solar collector manifold: a finite element and artificial neural network study, *Applied Thermal Engineering*, 303, 2026, 132183.
[34] Akbar, Y., Iqbal, J., Turabi, Y.U.U.B., Anwar, T., Alam, M.M., Magneto-radiative effects on thermal fields and irreversibility in a lid-driven wavy square enclosure with a central heater, *Journal of Thermal Analysis and Calorimetry*, 150(25), 2025, 21171-21184.
[35] Turabi, Y.U.U.B., Ahmad, S., Ahmad, S., Finite element and neural network modeling of thermal energy storage and entropy behavior in a wavy porous triangular enclosure with nano-encapsulated phase change materials, *Physics of Fluids*, 37(10), 2025, 102025.

Appendix

The steady two-dimensional incompressible Boussinesq equations used to obtain the dimensionless formulation are:

$$\partial u/\partial x + \partial v/\partial y = 0. \tag{A1}$$

$$u\partial u/\partial x + v\partial u/\partial y = -(1/\rho)\partial p/\partial x + \nu(\partial^2 u/\partial x^2 + \partial^2 u/\partial y^2). \tag{A2}$$

$$u\partial v/\partial x + v\partial v/\partial y = -(1/\rho)\partial p/\partial y + \nu(\partial^2 v/\partial x^2 + \partial^2 v/\partial y^2) + g\beta(T - T_c). \tag{A3}$$

$$u\partial T/\partial x + v\partial T/\partial y = \alpha(\partial^2 T/\partial x^2 + \partial^2 T/\partial y^2). \tag{A4}$$

The dimensionless variables are:

$$X = \frac{x}{L}, \quad Y = \frac{y}{L}, \quad U = \frac{uL}{\alpha}, \quad V = \frac{vL}{\alpha}, \quad P = \frac{pL^2}{\rho\alpha^2}, \quad \theta = (T - T_c)/(T_h - T_c). \tag{A5}$$

with $Pr = \nu/\alpha$ and $Ra = g\beta(T_h - T_c)L^3/(\nu\alpha)$. Substitution gives Eqs. (1)–(4) in the main text. The exact dimensionless boundary conditions used in the simulations are:

$$U = V = 0 \text{ on all solid boundaries.} \tag{A6}$$

$$\theta = \cos(\pi X) \text{ on the bottom wavy wall; } \theta = \cos(\pi Y) \text{ on the left wavy wall.} \tag{A7}$$

$$\theta = 0 \text{ on the right wavy wall; } n \cdot \nabla\theta = 0 \text{ on the top wall.} \tag{A8}$$

$$\text{On the rectangular block, } \theta = 0 \text{ in Case I and } \theta = 1 \text{ in Case II.} \tag{A9}$$

These expressions are identical to the COMSOL thermal conditions reported in Table 1. The cosine distributions are intentional. Here, 'periodic heating' denotes spatially periodic thermal forcing; $\theta < 0$ indicates $T < T_c$ relative to the selected reference temperature and does not represent a negative absolute temperature.

ORCID iD

Md. Aslam Hossain https://orcid.org/0009-0008-3178-6794

© 2026 Shahid Chamran University of Ahvaz, Ahvaz, Iran. This article is an open access article distributed under the terms and conditions of the Creative Commons Attribution-NonCommercial 4.0 International (CC BY-NC 4.0 license) (http://creativecommons.org/licenses/by-nc/4.0/).

How to cite this article: Rahman Md.S., et al. Thermal Performance Enhancement in Wavy Enclosures using Strategically Positioned Rectangular Blocks under Periodic Heating Conditions for Thermal Management Applications, *J. Appl. Comput. Mech.*, xx(x), 2026, 1–24. https://doi.org/10.22055/jacm.2026.49568.6081

Publisher's Note Shahid Chamran University of Ahvaz remains neutral with regard to jurisdictional claims in published maps and institutional affiliations.